

CYCLIC FATIGUE BEHAVIOUR OF WROUGHT AZ80
MAGNESIUM ALLOY FROM AUTOMOTIVE WHEEL

CYCLIC FATIGUE BEHAVIOUR OF WROUGHT AZ80
MAGNESIUM ALLOY FROM AUTOMOTIVE WHEEL

By Geoffrey Rivers

A Thesis

Submitted to the school of Graduate Studies

in Partial Fulfillment of the Requirements

for the Degree

Master of Applied Science

McMaster University

© Copyright by Geoffrey Rivers, January 2011

MASTER OF APPLIED SCIENCE (2011)

McMaster University

Materials Science and Engineering

Hamilton, Ontario, Canada

TITLE: Cyclic Fatigue Behaviour of Wrought AZ80 Magnesium Alloy
from Forged Automotive Wheel

AUTHORS: Geoffrey Rivers, B.Eng.

SUPERVISOR: Dr. Marek Niewczas

NUMBER OF PAGES: i – x, 1 – 69

Abstract

Wrought AZ80 magnesium alloy from a spoke of forged automotive wheel was subjected to high cycle fatigue to study its fatigue properties and to understand the relationship between the material substructure and fatigue life. The results reveal that in axial tension-compression S-N testing the spoke material exhibits an endurance limit of 98MPa and a sharp bend in the S-N curve. Fracture surface observation by SEM revealed rapid crack growth after crack nucleation with micro voids and angled secondary cracks throughout. XRD analysis revealed a strong material texture beneficial to basal slip activation before and after fatiguing, with small amounts of refinement after cycling and no signs of twinning. TEM observations of samples cycled at high stress and stresses above and below the endurance limit revealed a large difference in the dislocation substructures developed, which may relate to the sharp bend in the S-N curve.

Acknowledgements

The author would like to thank my supervisor Dr. Marek Niewczas for his support and expertise throughout the master program.

The author is also grateful to Dr. Feng Ju of the University of Alberta and Dr. Brad Diak of Queens University for their work leading up to this project. This study was supported by Auto21.

In addition, the author would like to thank the faculty, staff and fellow students of McMaster University, as so many contributed technical assistance, support and encouragement to this study.

Finally, my family, for everything they've done.

Table of Contents

Abstract.....	iii
Acknowledgements	iv
Table of Contents	v
List of Figures.....	vii
List of Tables	x
Chapter 1 – Introduction.....	1
Chapter 2 - Literature Review	3
2.1 Fatigue overview	3
2.1.1 Fatigue in general.....	3
2.1.2 Fatigue life determination	4
2.1.3 S-N curves.....	5
2.2 Fatigue failure mechanisms	6
2.3.1 Slip modes in magnesium	9
2.3.2 Dislocation behaviour	13
2.4 Fatigue behaviour of magnesium and its alloys	15
2.4.1 Fatigue of pure magnesium.....	15
2.4.2 Fatigue of magnesium alloys	16
2.4.3 Fatigue of AZ80 magnesium alloy	18
2.4.4 Microstructure influence on fatigue of magnesium alloys	20
2.4.5 Fracture behavior in fatigued magnesium alloys	21

2.5 Finite element analysis of wheel geometry.....	22
2.6 Tensile properties of wrought wheel material.....	24
2.7 Objective of the Work	24
Chapter 3 - Experimental Procedure.....	26
3.1 Sample preparation and details.....	26
3.2 S-N Fatigue testing of samples	28
3.2.1 Equipment and set up.....	28
3.2.2 Test specifications.....	29
3.3 Sample preparation for SEM and TEM studies	33
3.3.1 SEM sample preparation.....	33
3.3.2 TEM sample preparation.....	34
Chapter 4 - Experimental Results	37
4.1 S-N testing results	37
4.1.1 S-N curve	37
4.1.2 Accuracy of loading during testing.....	38
4.1.3 Anomalous results.....	38
4.2 SEM fracture surface observations	39
4.4 Texture analysis	46
4.5 TEM observation of microstructure	47
Chapter 5 - Discussion	58
Chapter 6 – Summary and Conclusions	66
References.....	68

List of Figures

Fig 2.1 - Diagram of plastic blunting process for fatigue crack growth. (Courtney, 2000)	7
Fig 2.2 - Fracture face in the fatigue crack region from a section of train rail showing (A) burnished section with fatigue striations removed by damage during fatigue, (B) region of plastic blunting controlled growth and (C) region of final rupture by rapid crack growth (The Transportation Safety Board of Canada, 2008).....	8
Fig 2.3 - Slip systems in HCP crystals (a) Basal, prismatic, and pyramidal slip systems with $\langle a \rangle$ Burgers vector, and (b) four possible pyramidal slip planes with $\langle c+a \rangle$ Burgers vector. (Yoo, 1981).....	10
Fig 2.4 - Common Slip Planes in Mg (courtesy of Fumiaki Hiura, 2010)	12
Fig 2.5 - CRSS versus Temperature for Magnesium, (courtesy of Fumiaki Hiura, 2010)	12
Fig 2.6 - Evolution of the dislocation source mechanism for the $\langle c + a \rangle$ pyramidal slip system: (a) cross-slip of $\langle a \rangle$ dislocation, (b) formation of $\langle c + a \rangle$ attractive junction, and (c) cross-slip of $\langle c + a \rangle$ dislocation. (Yoo, Morris, Ho and Agnew, 2002).....	15
Fig 2.7 - FEA of Von Mises stresses in wheel geometry, with tire hidden (Ju, 2008)	23
Fig 3.1 - Cross-section of forged AZ80 wheel. Detail (A) shows location and orientation of sample sets in wheel, with spoke section samples taken from location i).....	26
Fig 3.2 - Side view of cylindrical fatigue sample showing dimensions	27
Fig 3.3 - Diagram of selection and preparation for fracture surface SEM	34
Fig 4.1 - Total life S-N curve for spoke material of wrought AZ80 magnesium alloy wheel.....	37

Fig 4.2 - Plot of Peak Tensile Stress Applied vs Cycles Completed for samples used in construction of S-N curve	38
Fig 4.3 - Side view of surface fracture for 135MPa stress amplitude sample	40
Fig 4.4 - Surface Texture near crack nucleation point on 135MPa sample	41
Fig 4.5 - Surface Texture near crack nucleation point on 99MPa sample	42
Fig 4.6 - Angled secondary cracking in 135MPa sample	43
Fig 4.7 - Smooth region near crack nucleation point in fracture surface of 150MPa sample	44
Fig 4.8 - Transition region towards increased step size in fracture surface of 150MPa sample	45
Fig 4.9 - Side view of surface fracture for 150MPa stress amplitude sample	45
Fig 4.10 - Pole figured collected from samples fatigued at a) 150MPa, b) 99MPa, c) 98MPa and an as-forged sample, d).....	46
Fig 4.11 - Bright Field TEM of 150MPa sample showing densely packed loop dislocations and dislocation debris	48
Fig 4.12 - Dark field TEM of 150MPa sample showing lattice-like dislocation array	49
Fig 4.13 - Dislocation loops observed in bright field TEM of 99MPa sample.....	50
Fig 4.14 - Dislocation loops observed in TEM dark field of 99MPa sample	51
Fig 4.15 - Bright field TEM of dislocation substructure in 99MPa sample	52
Fig 4.16 - Dark field TEM showing dislocation network in of 99MPa sample.....	53
Fig 4.17 - Dark field TEM showing small dislocation debris and isolated dislocations in 98MPa sample.....	54

Fig 4.18 - Dark field TEM of 98MPa sample showing distended dislocation segments and sparse dislocation loops 55

Fig 4.19 - Dark field observations of aligned dislocations near grain boundary in 98MPa sample 56

Fig 4.20 - Dark field of dislocations clustering at subgrain boundary in 98MPa sample. 57

List of Tables

Table 2.1 - Independent modes of deformation in HCP crystals, (Yoo, 1981)	10
Table 2 - Properties of some hexagonal close-packed metals at 300K (Hull and Bacon, 2001)	11
Table 2.3 - Nominal chemical composition (wt%) of the magnesium alloys studied by Strivatsan, Wei and Chang.....	17
Table 4.1 - Testing condition and fatigue life results for samples considered invalid for S-N analysis	39

Chapter 1 – Introduction

Utilization of magnesium and magnesium alloys has increased substantially in recent years, particularly in the aircraft and automotive industry, because of the advantageous properties of these materials over the alternative materials. The properties that make Mg-based alloys attractive for many applications are (Kainer, 2003)

- Lowest density of all construction grade metals at 1.8g/cm³
- High strength to density ratio
- Excellent castability and suitability for die casting
- Machineability at high cutting speeds
- Recyclability

Magnesium alloys are ideal for the production of high strength low weight parts, such as structural engine components. However, some parts, such as automotive wheels are not suitable for casting, and are produced by means of forging processes. Typically magnesium alloys display poor formability, however, this issue can be mediated by a well-designed hot forging process, allowing the production of lightweight automotive wheels. Such a process was previously used to produce a magnesium AZ80 alloy automotive wheel, which is now being tested for its mechanical and material properties. For high use dynamic components, the failure by cyclic fatigue becomes a concern. More than 90% of material failures during exploitation are due to fatigue (Sachs, 2004). Literature pertaining to the fatigue of magnesium AZ80 is limited and shows high variability in the observed fatigue behaviour. Additionally, fatigue properties are

microstructure dependent and the process of forging of a complex part, such as a wheel, induces variation in the microstructure throughout the forged part. As such, it can be expected that the fatigue behaviour found throughout the wheel will vary. The current understanding of the fatigue properties of AZ80 alloys is insufficient to predict the fatigue life of the wheel, thus necessitating present studies of the fatigue behavior of AZ80 alloy taken from the spoke of a forged wheel.

Chapter 2 - Literature Review

2.1 Fatigue overview

2.1.1 Fatigue in general

Fatigue refers to changes in the properties of materials which occur due to repeated applications of stresses or strains, generally leading to cracking or failure. (Geneva, 1964) The fatigue failure is of interest as fatigue occurs at lower stress and strain amplitudes than would be required to induce static failure. Fatigue failure often occurs in the elastic loading range under stress much smaller than the yield stress of the material. Fatigue is caused by accumulation of small-scale defects over a number of loading cycles, including the nucleation and growth of cracks or voids, which eventually leads to failure. Conditions for crack nucleation and propagation are strongly influenced by a range of mechanical, microstructural and environmental factors, which must be considered while predicting the fatigue life. Fatigue occurs in several stages:

- 1) Substructural and microstructural changes which nucleate permanent damage
- 2) Nucleation of microscopic voids or cracks
- 3) Growth and coalescence of microscopic flaws to form dominant cracks
- 4) Stable crack growth of the dominant crack
- 5) Structural instability or complete fracture

(S. Suresh, 1991)

2.1.2 Fatigue life determination

Determination of the fatigue life is dependent on which stage failure of the material is considered. In some cases, the number of cycles required to nucleate cracks and to induce the crack growth is considered the fatigue life. In the case of “total-life” approaches, the fatigue life is considered to be defined by the complete fracture or failure of the material. In other cases, a defect-tolerant approach, which assumes that all manufactured parts inherently contain flaws, in which non-destructive observation and proof testing by cycling a component at stress or strain amplitudes above service conditions are used to estimate the largest possible undetected crack or flaw and from this provide an estimate of the safe service life of the component. (S. Suresh, 1991)

Classical methods of fatigue testing involve the characterization of total fatigue life to failure in terms of the cyclic stress range or the cyclic strain range. In these approaches, the number of stress or strain cycles necessary to induce complete fatigue failure, in initially uncracked samples, is estimated under controlled amplitudes of cyclic stress or strain. (S. Suresh, 1991)

Classical stress and strain-based methods typically represent design against the initiation of a dominant fatigue crack. Testing methods focused on stress or strain amplitudes high enough to produce appreciable plastic deformation and a low number of cycles to failure are referred to as low-cycle fatigue. These are primarily characterized in terms of strain range, and are typically used to study the initiation and early growth stages

of a crack forming in the fully plastic region produced by a stress concentrator on a part. Conversely, methods focused on stresses or strains low enough to result in high numbers of cycles to failure and producing low amounts of plastic deformation or even elastic deformation, are referred to as high-cycle fatigue testing and usually characterized in terms of their stress range. Low-cycle fatigue methods are often used when studying the influences of surface treatments, environmental conditions or microstructure on the initiation, growth and final fracture of a dominant fatigue crack. (S. Suresh, 1991)

2.1.3 S-N curves

The most common method of characterizing high-cycle fatigue life behavior is through constructing the S-N curve, where multiple samples of a material are fatigued to failure under stress control mode and the stress amplitude is plotted against the number of cycles to failure. The loading of samples in S-N testing is typically performed under conditions of sinusoidal and “fully reversed” stress, in which the peak stress amplitude is applied equally in alternating tension and compression once per cycle along a sinusoidal loading profile. This test represents a powerful tool by which fatigue life of a material tested under a set of conditions can be easily characterized and compared to that of other materials and conditions. The obtained curve allows determination of the endurance limit of the material, defined as the stress amplitude below which failure due to fatigue effectively never occurs. In the case of some materials, there is no well-defined endurance limit, in which case the limit is defined as the stress at which the material survives 10^7

cycles without failure. The transition to the endurance limit also varies between materials and conditions, and is indicative of the stress sensitivity of the processes inducing fatigue damage within the material.

2.2 Fatigue failure mechanisms

Localized damage accumulates during fatiguing, even below its yield stress σ_y , because of the influence of localized stress concentrators such as part geometry or small scale defects, which act to locally increase the stress beyond the applied stress. Features such as sharp notches, corners or cracks disrupt idealized material continuum, forcing stress fields to deform around the disruption, which results in higher stress field densities in proximity to the feature. Therefore the size, orientation, location and equivalent radius at the stress concentrating edges of such a feature affect how it concentrates the stresses applied to a part, with larger sizes and smaller edge radii producing larger concentrations. Similar behavior, on a smaller scale, is found around grain boundaries, micro voids, inclusions and other disruptions in the material continuum.

In cyclic fatigue, once nucleated, the crack growth typically occurs in steps over a number of cycles due to a plastic crack tip blunting process. The stress concentration at the crack tip during the tensile portion of a cycle causes the crack tip to grow, which lengthens the crack, while simultaneously causing the crack tip radius to increase, as

illustrated in Fig 2.1. This blunting decreases the stress concentration caused by crack geometry, reducing the local stress and stalling the growth of the crack tip. When the loading cycle enters its compressive or lower stress period, the crack tip radius is reduced, raising the tensile stress concentration factor again. As such, from cycle to cycle, the crack tip typically grows by cycling through this growth and blunting process, until eventually the crack has grown to a size such that the local tensile stress at the crack tip is high enough to induce rupture in the sample, and the crack enters an unstable growth phase where it fractures the remaining material very rapidly. However, under favorable conditions, a nucleated crack may grow rapidly over a relatively small number of cycles, utilizing favorable microstructure to propagate in a semi-brittle manner. In this case, nucleation or growth of the crack tip may be delayed until the fatiguing process develops a suitable material microstructure, which facilitates crack propagation. In both instances, the crack will grow until the stress on the remaining section is high enough that it undergoes rupture through rapid crack growth.

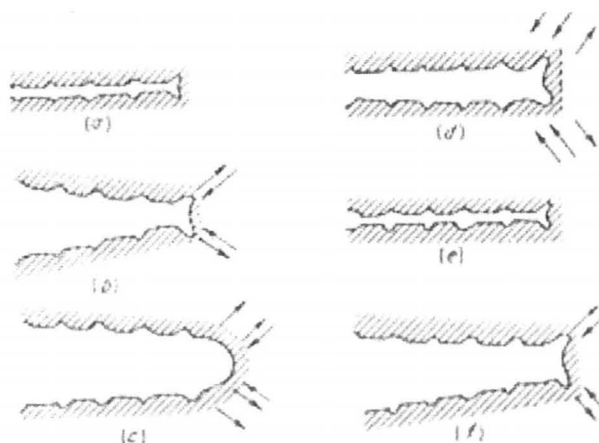


Fig 2.1 - Diagram of plastic blunting process for fatigue crack growth. (Courtney, 2000)

Due to the deformation processes occurring during a plastic blunting controlled crack growth period, the produced fracture surface typically contains striations on the surface texture, as seen in Fig 2.2. The distance between these surface striations denotes the length of crack growth which occurred in that particular cycle, while the striation orientation can be used to determine the initial crack nucleation point in some cases.

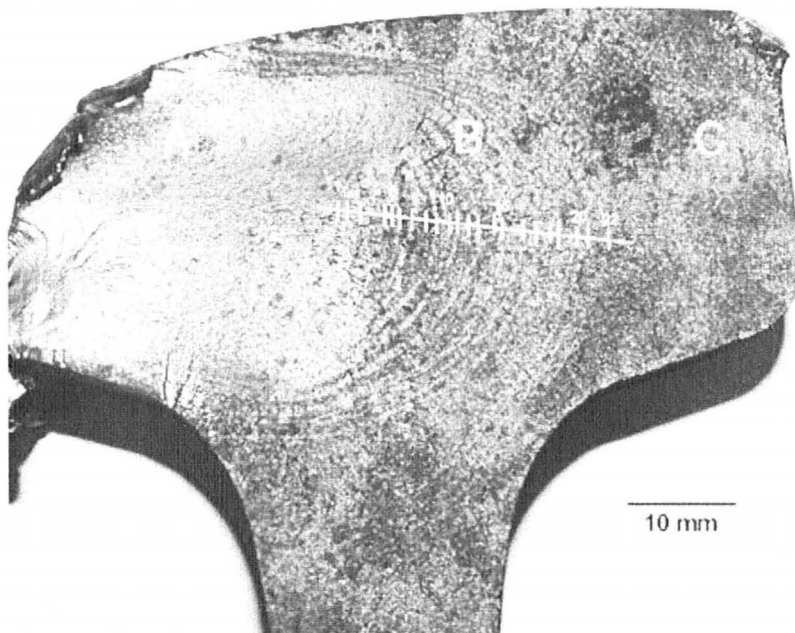


Fig 2.2 - Fracture face in the fatigue crack region from a section of train rail showing (A) burnished section with fatigue striations removed by damage during fatigue, (B) region of plastic blunting controlled growth and (C) region of final rupture by rapid crack growth (The Transportation Safety Board of Canada, 2008)

2.3 Dislocations

2.3.1 Slip modes in magnesium

Magnesium has a hexagonal closed packed structure (HCP) and ABAB.... packing sequence. The c/a ratio of the unit cell of magnesium is 1.623, very close to an ideal HCP lattice ($c/a=(8/3)^{1/2}=1.633$). Possible slip systems of HCP crystals are listed in Table 2.1 and shown in Fig 2.3. The (0001) basal plane of HCP crystals is close-packed and it includes three close-packed directions of $\langle 11\bar{2}0 \rangle$. Unit cell \mathbf{a} -vectors in the basal plane along the $\langle 11\bar{2}0 \rangle$ represent the shortest lattice vectors, therefore the most common slip system in HCP lattice is the basal slip system $\{0001\}\langle 11\bar{2}0 \rangle$. The system is often termed as basal $\langle \mathbf{a} \rangle$ slip. As there are no ideally close-packed HCP metals, and as such, the lattice parameter ratio c/a usually deviates from the ideal $c/a = 1.633$, some HCP metals such as titanium and zirconium preferentially undergo $\langle \mathbf{a} \rangle$ slip in the $\{10\bar{1}0\}$ prismatic plane. The c/a ratios of several HCP metals, including magnesium, are shown in Table 2.2, along with the preferred slip at 300K.

Table 2.1 - Independent modes of deformation in HCP crystals, (Yoo, 1981)

Direction	Plane	Crystallographic Elements	Number of Independent Mode
	Basal	$(0001)\langle 11\bar{2}0 \rangle$	2
$\langle a \rangle$	Prismatic	$\{10\bar{1}0\}\langle 11\bar{2}0 \rangle$	2
	Pyramidal	$\{1\bar{1}0l\}\langle 11\bar{2}0 \rangle$	4
$\langle c \rangle$		$\{hki0\}[0001]$	
$\langle c+a \rangle$	Pyramidal	$\{hkil\}\langle 11\bar{2}3 \rangle$	5
Twinning		$\{K_1\}\langle \eta_1 \rangle$	0-5

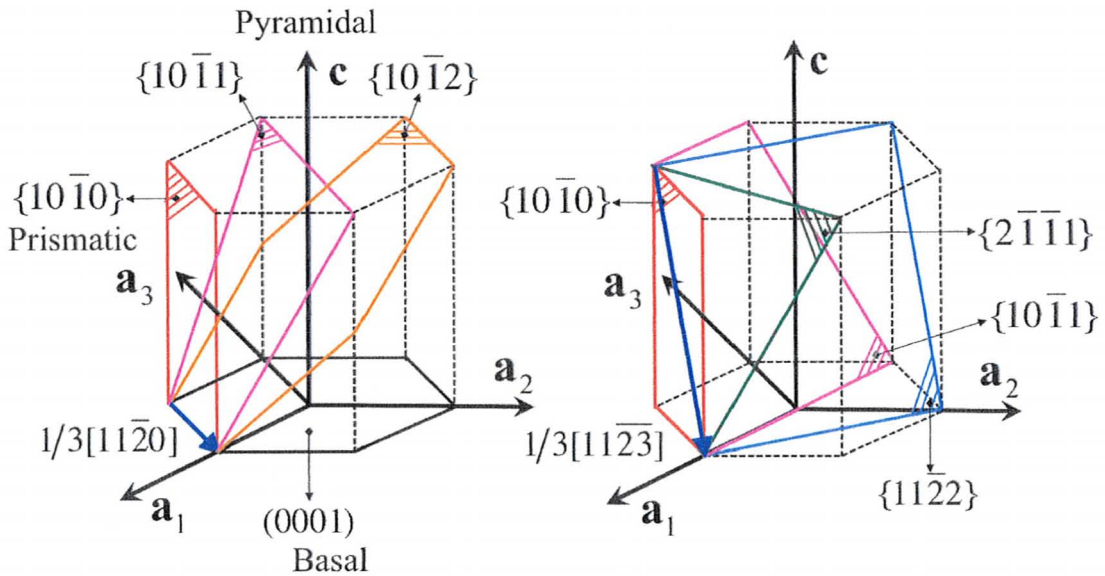


Fig 2.3 - Slip systems in HCP crystals (a) Basal, prismatic, and pyramidal slip systems with $\langle a \rangle$ Burgers vector, and (b) four possible pyramidal slip planes with $\langle c+a \rangle$ Burgers vector. (Yoo, 1981)

Table 2 - Properties of some hexagonal close-packed metals at 300K (Hull and Bacon, 2001)

Metals	Be	Ti	Zr	Mg	Co	Zn	Cd
c/a ratio	1.568	1.587	1.593	1.623	1.628	1.856	1.886
Preferred slip	Basal	Prism	Prism	Basal	Basal	Basal	Basal

In addition to basal and prismatic $\langle a \rangle$ slip, HCP materials deform by $\langle a \rangle$ and $\langle c+a \rangle$ type slip on pyramidal planes. In magnesium and magnesium alloys basal and prismatic $\langle a \rangle$ slip and 2nd order pyramidal $\langle c+a \rangle$ type slip with the $a/3 \langle 11\bar{2}\bar{3} \rangle$ Burgers vector are primarily considered, illustrated in Fig 2.4. A plot of the temperature dependence of the critical resolved shear stress (CRSS) for each of these slip systems is shown in Fig 2.5. CRSS is the minimum stress required to initiate slip on a slip plane in a given direction. For magnesium, the basal $\langle a \rangle$ slip system is the dominant deformation process at room temperature, as the CRSS for $\langle a \rangle$ prismatic and $\langle c+a \rangle$ pyramidal are considerably higher than that of basal $\langle a \rangle$. In order to satisfy Von Mises' criterion, (Von Mises, 1928) a material undergoing deformation must have minimum five independent slip systems so that every grain in a polycrystalline material can deform to accommodate the deformations of neighbouring grains. Basal $\langle a \rangle$ slip only supplies two independent slip systems, as does prismatic $\langle a \rangle$, and due to the difference in CRSS values, prismatic $\langle a \rangle$ slip is not easily activated in room temperature deformation. Second order pyramidal $\langle c+a \rangle$ slip may contribute to the deformation along c-axis and, itself, has five independent slip modes, though the CRSS value for the plastic flow is quite high. As such, other processes such as $\{10\bar{1}2\}$ twinning, which have CRSS values lower than prismatic

and second order pyramidal slip systems and/or development of kink bands, may become active and may supply missing deformation components to satisfy five independent slip systems.

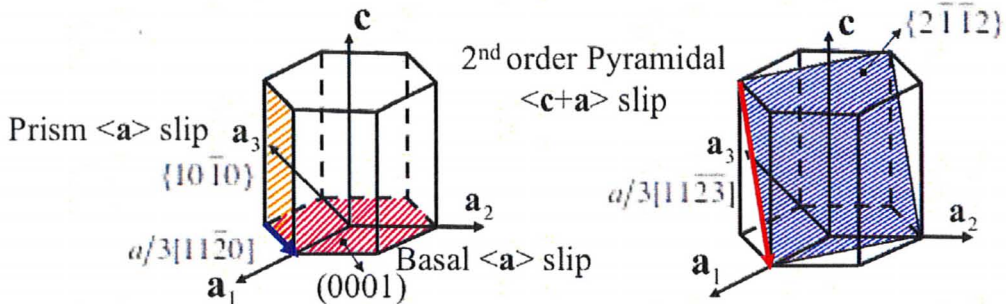


Fig 2.4 - Common Slip Planes in Mg (courtesy of Fumiaki Hiura, 2010)

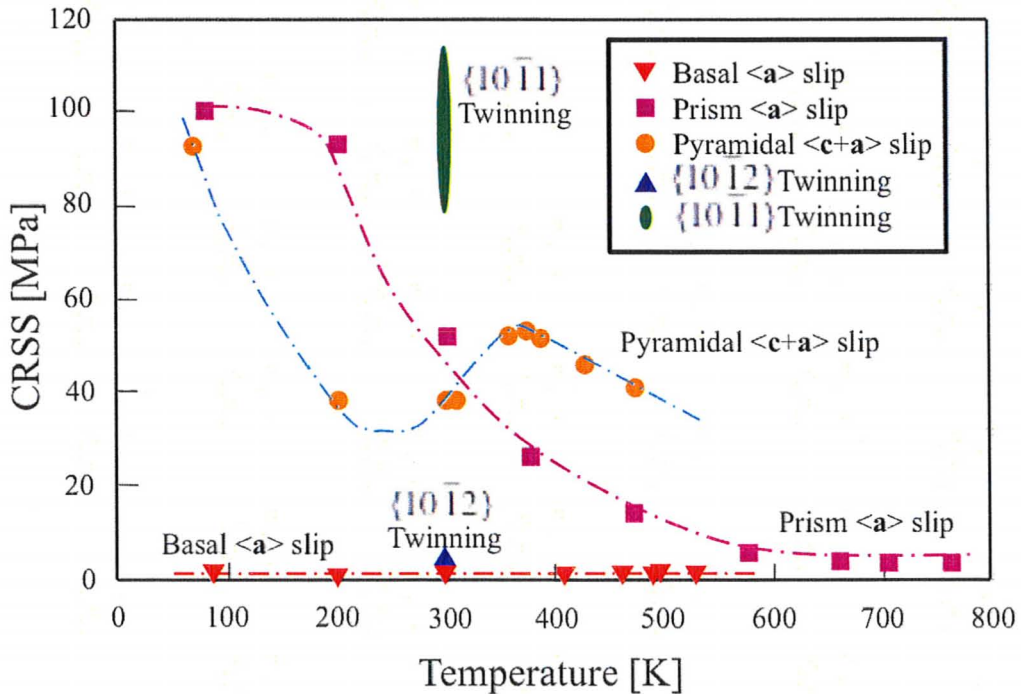


Fig 2.5 - CRSS versus Temperature for Magnesium, (courtesy of Fumiaki Hiura, 2010)

2.3.2 Dislocation behaviour

Dislocations are localized defects in the crystal lattice of a material, which distort the crystal lattice, and move under the influence of applied stress and act as “carriers” of the deformation process.

The distortion of the crystal lattice caused by a dislocation creates a characteristic stress state in the material containing tensile and compressive stress fields, which interact with other local stress fields, exerting a force on other dislocations. The external stress applied to the lattice causes the dislocation to move along a suitable slip plane and along suitable crystallographic direction. Dislocations act as stress concentrators and are carriers of the slip deformation along the involved slip plane.

As each dislocation is associated with a stress field, and in turn influenced by other stress fields, dislocations will interact with one another when in proximity. Favorably arranged dislocations of opposite orientation can merge and annihilate. Dislocations lying on the same glide plane that are of the same type repel each other, causing them to arrange in a configuration that produces large back stresses in the slip plane. Such processes commonly occur at grain boundaries, where dislocation glide is impeded by the misorientation of the crystal lattice across the grain boundary. Substructures such as these may act to increase stress concentration in a region of material, or may also decrease the total stress concentration in a region by artificially increasing the apparent defect radius of an existing concentrator.

Dislocations will also interact with dislocations oriented on other slip systems through their stress fields, which produces back stress on the mobile dislocation as it cuts through the other dislocation substructures. The resistance may be high enough so that large sections of a mobile dislocation segment can become pinned and immobile.

In a material undergoing cyclic loading such that it is not accumulating damage the dislocations simply glide back and forth in completely reversible deformation. However, at stress amplitudes sufficient to cause accumulated damage, the dislocations may undergo unrecoverable slip processes. Under sufficient stress conditions it is possible for similarly oriented dislocations to overcome the mutual repulsion of their stress fields and merge and form a micro-void in the material, which can then act as a nucleation point for cracks. Dislocations can cross slip onto other planes or other slip systems, and can interact with dislocations of other Burgers vector to form dislocation segments which operate on different slip systems, as shown in Fig 2.6. This produces structures that cannot be reversed by the opposite phase of the cyclic loading.

Dislocations which are pinned at points either by particles in the lattice acting as barriers or by dislocations on other slip systems will have the segment between the points bow outwards in the direction of slip. However, with sufficient applied stress this bowing can cause the formation of a closed loop of dislocation, which is irrecoverable in cyclic loading.

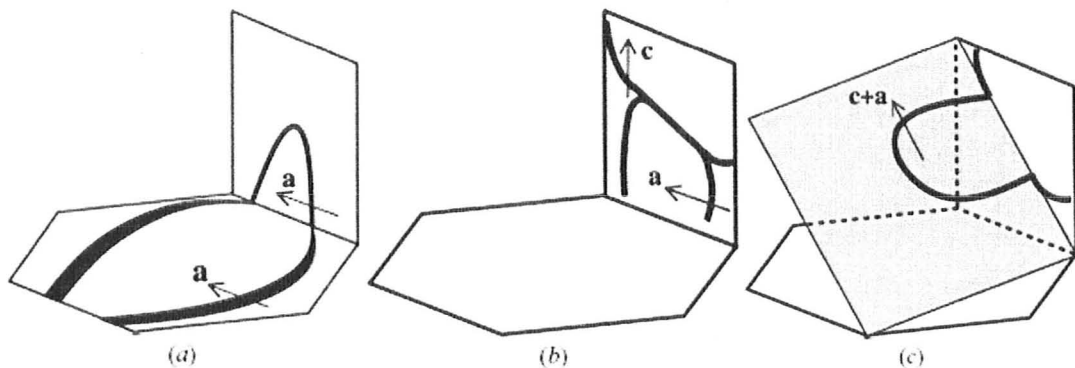


Fig 2.6 - Evolution of the dislocation source mechanism for the $\langle c + a \rangle$ pyramidal slip system: (a) cross-slip of $\langle a \rangle$ dislocation, (b) formation of $\langle c + a \rangle$ attractive junction, and (c) cross-slip of $\langle c + a \rangle$ dislocation. (Yoo, Morris, Ho and Agnew, 2002)

2.4 Fatigue behaviour of magnesium and its alloys

2.4.1 Fatigue of pure magnesium

Stevenson and Vander Sande conducted strain controlled fatiguing tests on 99.95+ purity magnesium single crystals, comparing fatigue life and slip behaviour to the crystal orientation with respect to the tensile axis. Results showed that the magnesium primarily deformed by slip processes, although both kink and twinning bands were observed in some cases. Observation of the slip bands by TEM indicated that in all samples, independent of the testing orientation, some degree of duplex slip, the process by which the material slips on two or more planes simultaneously, had occurred. This behavior did however loosely correlate to the applied strain amplitude such that low strain amplitudes produced predominately single slip deformation, while high strain amplitudes produced dislocation substructures in which duplex slip was more prominent. (Stevenson and Vander Sande, 1974)

Hutchinson and Barnett studied single crystal of pure magnesium alongside polycrystalline magnesium alloys of varying composition. Analysis showed that as dislocation density increases, prismatic glide planes become increasingly favorable with respect to the preference for basal glide. In polycrystalline materials grain boundaries act to block slip bands, raising the value of the plastic yielding stress with respect to single crystals by inducing back pressures in dislocation glide. As noted by Hutchison and Barnett, the hardening contributions are not proportional to the CRSS values, but are additive. Thus CRSS values from single crystal results do not directly reflect the applied shear stresses that are necessary to activate different slip modes in polycrystalline materials. (Hutchinson and Barnett, 2010)

2.4.2 Fatigue of magnesium alloys

Srivatsan, Wei and Chang studied the fatigue of several magnesium alloys under strain controlled axial fatigue conditions. The nominal compositions of these alloys are listed in Table 2.3, and samples were produced through planar flow casting in a vacuum environment. Results showed that under strain control, cyclic stress response of the rapidly solidified magnesium alloys revealed initial softening followed by stability for most of fatigue life, with fatigue eventually culminating in rapid softening prior to failure at the higher cyclic strain amplitudes and concomitant higher response stress. Softening prior to failure was attributed to the formation, growth and coalescence of cracks in the sample, reducing the load carrying capacity of the sample structure. (Srivatsan, Wei and Chang, 1997)

Table 2.3 - Nominal chemical composition (wt%) of the magnesium alloys studied by Strivatsan, Wei and Chang

Alloy	Element			
	Al	Zn	Nd	Mg
1	5.72	2.96	6.05	Balance
2	4.89	4.36	5.81	Balance
3	4.96	4.75	5.43	Balance

Chen et al. studied the fatigue behavior of as-extruded AM50 under strain controlled axial loading conditions, which exhibited a solid solution α -phase and a harder β -phase composed of $Mg_{17}Al_{12}$. Analysis showed pronounced anisotropic deformation behavior in the tensile and compression directions at high strain amplitudes. (Chen et al, 2007)

Nan and colleagues performed studies on the behaviour of magnesium AZ31 produced by extrusion under stress-controlled rotating-bending fatigue conditions. This alloy formed three phases of varying hardness. Phase A composed of magnesium matrix, phase B composed of $Mg_{32}(Al,Zn)_{49}$, and phase C comprised of $Mg_{17}Al_{12}$, with phases A and B layered in a lamellar structure parallel to the extrusion direction. Phase C formed as a precipitate grain inside of phase B. Testing revealed a sharp bend on the S-N curve of AZ31, leading to a well-defined endurance limit. (Nan, Ishihara, Goshima and Nakanishi, 2004) Tokaji and colleagues performed fatigue life characterization of an AZ31 alloy produced by rolling, using axially loaded stress controlled fatigue in lab air conditions.

This AZ31 showed no sharp bend in the S-N curve, and a well-defined endurance limit of only 50 MPa. Non-propagating cracks were found on the surface of the endurance limit sample. (Tokaji et. al. 2004) While studying the fatigue behavior of both extruded and annealed AZ31 alloy under strain controlled conditions, Matsuzuki and Horibe observed twinning as being the predominant deformation mechanism at higher plastic strain amplitudes, while dislocation slips are the primary mode of deformation at lower plastic strain amplitudes for the same orientations. (Matsuzuki, Horibe, 2008)

The team of Li et al. performed a comparison between the fatigue behaviour of two magnesium alloys, AZ91 and AE42, each in die cast and solution heat-treated forms, under strain controlled axial loading conditions. Analysis showed that solution treatment substantially improved the fatigue life of AZ91 compared to its die cast form, while the same treatment caused the fatigue life of magnesium AE42 to decrease compared to the die cast samples. (Li et al., 2005) This serves as an example that the fatigue behavior of other magnesium alloys should not be considered predictive, and are simply valued for comparative purposes.

2.4.3 Fatigue of AZ80 magnesium alloy

Cyclic fatigue behavior of extruded magnesium AZ80, under axially loaded strain controlled fatigue conditions was studied by Zenner and Renner, alongside samples of magnesium alloys AZ91, AE42 and AZ31. Results exhibited a pronounced anisotropy in the AZ80 with respect to the material strength when comparing the tensile and

compressive loading conditions. (Zenner and Renner,2002) Shahzad, Eliezer, Gan, Yi and Wagner performed testing on extruded magnesium AZ80 and ZK60 alloys, varying the extrusion temperature to produce samples varying in average grain size to illustrate the influence of average grain size on the alloy fatigue life and fatigue behavior. Fatigue was performed in stress controlled mode axial fatigue with a tensile axis parallel to the extrusion axis. In this instance the S-N curve of the AZ80 did not exhibit a sharp bend or a well-defined endurance limit. (Shahzad, Eliezer, Gan, Yi and Wagner, 2007)

Hilpert and Wagner fatigued samples of extruded magnesium AZ80 containing only solid-solution α -phase material with an average grain size of 30 μm in laboratory air conditions, as well as under corrosive environments, under stress controlled axial-loaded fatigue conditions. Samples in this study were cut such that the tensile axis of one set was parallel to the extrusion direction, while the tensile axis of the other set was oriented perpendicular to the extrusion axis, in order to study the influence of microstructure orientation on the sample fatigue properties. Regardless of orientation, the S-N curves collected did not exhibit a sharp bend for this material. (Hilpert and Wagner, 2000) Zhang, Lindemann, Kiefer and Leyens studied the influence of mechanical surface treatments on the fatigue behaviour of wrought magnesium AZ80, using hourglass round samples cut from a forged rectangular bar containing only solid-solution α -phase material with an average grain size of 30 μm , tested under load controlled rotating bending fatigue. The samples had been surface treated with shot peening by different peening mediums and conditions, or by roller burnishing under different rolling forces. For both the shot peened

and roller burnished samples, the fatigue behavior was influenced positively by the treatment compared to untreated samples. However neither the untreated or treated samples exhibited a well-defined endurance limit or sharp bend on the S-N curve. (Zhang, Lindemann, Kiefer and Leyens, 2005) (Zhang, Lindemann. 2005)

2.4.4 Microstructure influence on fatigue of magnesium alloys

As the processing method of a material produces microstructures that influence the fatigue life and behaviour, Zúberová and co-workers studied the fatigue and tensile behaviour of cast, hot-rolled, and severely plastically deformed AZ31 magnesium alloy under stress controlled axial fatigue conditions in laboratory air. Analysis of S-N curves revealed a strong dependence of the endurance limit and fatigue life on the production method and by extension the microstructure present, while each method resulted in a S-N curve containing a sharp bend located at a different stress amplitude, and varying fatigue lives. (Zúberová, et al, 2007) In their study of extruded and annealed AZ31 Matsuzuki and Horibe noted that Extruded AZ31 showed slightly longer fatigue life than annealed AZ31, and suggested that this was due to the materials having different dislocation densities. (Matsuzuki, Horibe, 2008) The results of studies into extruded AZ31 by Nan and colleagues showed the microstructure of material was likely the cause of the sharp bend in the resulting S-N curve. (Nan, Ishihara, Goshima and Nakanishi, 2004)

By varying processing temperature to control the average grain size in extruded AZ80 alloy, Shahzad et al. found appreciable changes in fatigue behavior relating to

relatively small changes in average grain size. It was found that a decrease in average grain size typically resulted in an increase in the fatigue life, with a decrease of $7\mu\text{m}$ to $5\mu\text{m}$ average grain size resulted in an increase from approximately 125MPa to 150 MPa stress amplitude for the apparent endurance limit. However, regardless of grain size the S-N curves for AZ80 all shared the common minimum fatigue life of approximately 2×10^4 cycles at approximately 175MPa stress amplitude. (Matsuzuki, Horibe, 2008) In their study of the corrosion fatigue characteristics of extruded AZ80, Hilpert and Wagner varied the orientation of the fatigue loading axis with respect to the extrusion axis of the material in order to study the influence of microstructure. While neither orientation contained a distinct endurance limit or sharp bend in the S-N curve they did exhibit differing fatigue life behaviour, with the radial direction exhibiting a lower apparent endurance limit, and lower fatigue life than the extrusion-axis loaded material. This implies a strong influence on fatigue behaviour by AZ80 microstructure. (Hilpert and Wagner, 2000)

2.4.5 Fracture behavior in fatigued magnesium alloys

In the study by Chen et al. on the fatigue behaviour of extruded magnesium AM50 alloy, it was found that cracking initiated trans-granularly at the surface and then propagated in trans-granular mode. Secondary cracking and microscopic voids were seen on the fracture surface. (Chen et al, 2007) In contrast the study of extruded AZ31 by Nan and colleagues found that fracture began as an intergranular crack in the crystal lattice of the phase C material, where it propagates until reaching the grain boundary where its

growth is impeded over a large number of cycles by the B-phase material. This stationary crack was suggested as being the cause of the well defined endurance limit and sharp bend in the S-N curve of extruded AZ31, and a parallel drawn to a similar stationary crack seen at the endurance limit of carbon steels which also exhibit a sharp bend in their S-N curve. (Nan, Ishihara, Goshima and Nakanishi, 2004) Tokaji and colleagues in their study of AZ31 fatigue fracture also found these non-propagating cracks, although in this case there was no sharp bend in the S-N curve. (Tokaji et. al. 2004) When studying the fatigue and fracture properties of several magnesium alloys Srivatsan, Wei and Chang found on the fracture surface of all alloys a region of stable crack growth, and a region of growth by tensile overload. The stable crack growth region contained microscopic cracks extending along grain boundaries running parallel to the major stress axis, with high strain amplitudes producing a large amount of cracking. Low strain amplitudes produced fracture surfaces that were characteristically flat and featureless with relatively less cracking. The overload region surface revealed ductile failure features including small voids and dimples of various sizes, interspersed with brittle failure and fracture along grain boundaries. (Srivatsan, Wei and Chang, 1997)

2.5 Finite element analysis of wheel geometry

In previous work connected with the AZ80 magnesium alloy wheel project, Finite Element Analysis (FEA) has been carried out on wheel geometry of a prototype wheel, to determine the weakest structural points in designed wheel structure (Ju, 2008). A peak

Von Mises stress of 21.45 MPa has been found to be located in the rim section of the wheel near the junction of the rim and spokes. In the spoke section the peak Von Mises stresses of 18MPa was found at the rim adjacent section of the spokes and 14MPa near the midpoint of the length of the spoke, as seen in Fig 2.7. Analysis was performed with the wheel loaded with 800Kgf by bearing contact in hub, and the wheel fitted with a model of a rubber air tire of appropriate size with 32psi internal pressure on a flat surface designated as unyielding.

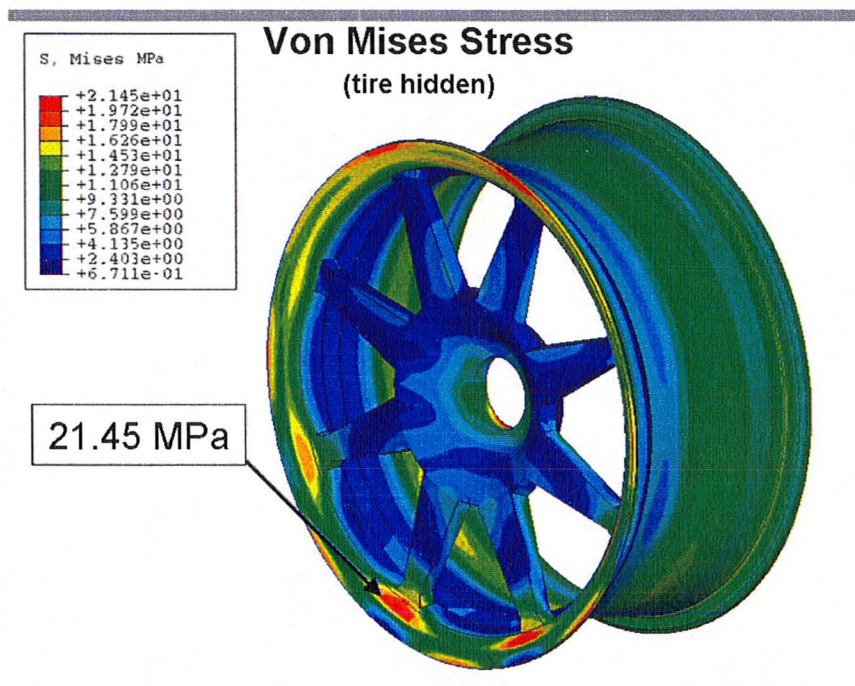


Fig 2.7 - FEA of Von Mises stresses in wheel geometry, with tire hidden (Ju, 2008)

2.6 Tensile properties of wrought wheel material

Tensile tests have been carried out on samples taken from the spoke sections of a wrought AZ80 magnesium alloy wheel produced for this project (Diak, 2009). The spoke material tensile yield true stress is 110MPa with a true yielding strain of approximately 0.005. This represents a tensile engineering yield stress $\sigma_{0.2\%,e}$ of approximately 109MPa. These tests were performed with the samples machined such that their tensile axis was parallel to the long axis of the spoke.

2.7 Objective of the Work

The importance of S-N testing to the characterization of fatigue life was discussed in section 2.1.3. The important role in fatigue testing of manufactured components has been known for decades, and the influence on manufacturing process produced microstructure has been studied by S-N testing. Although many magnesium alloys have been studied, there is little information on the fatigue influence of forged microstructure in magnesium AZ80 alloy. Therefore, this study represents a valuable step to understanding the influence of forged microstructure on fatigue properties and behavior of forged magnesium AZ80 alloy.

Other studies about the fatigue of magnesium alloys, and on AZ80 were described in section 2.4. Many have shown microstructure dependence of the fatigue behaviour, relating microstructure orientation, grain size, and surface treatment effects to the fatigue

life. However there remains limited investigation into the mechanisms involved, and little work done on the variation of fatigue behaviour throughout complex shaped magnesium alloy parts produced through forging processes. Such work would be beneficial to industry as forging process design could be controlled to produce fatigue resistance favorable microstructure.

Purpose of this study is to provide experimental data on the fatigue life behaviour of AZ80 material from the spoke of a wheel produced through a hot forging process and to understand the relationship between microstructure and fatigue behavior of AZ80 alloy used in the automotive wheel.

Chapter 3 - Experimental Procedure

3.1 Sample preparation and details

All samples tested were machined from a prototype wheel produced by the hot forging process and are grouped into four sets. Each set represents one of four positions in the prototype wheel, from which the samples in that set were machined. It is by comparing the fatigue life results and microstructure of the four sets that it will be possible to analyze the effects of the hot forging process on the alloy's fatigue properties. Fig 3.1 shows a cross section of the designed wheel, showing the origin position and orientation of each sample set. All samples for this project were machined at Queens University.

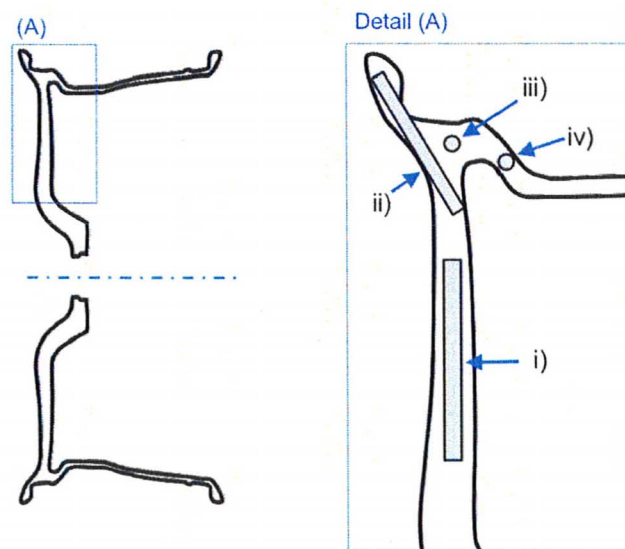


Fig 3.1 - Cross-section of forged AZ80 wheel. Detail (A) shows location and orientation of sample sets in wheel, with spoke section samples taken from location i)

The samples are machined to be cylindrical, with a reduced diameter section acting as the gage length. The transition between the gage section and the wider grip sections is machined as a gentle curvature, intended to avoid the inclusion of a stress concentration factor in proximity to the gage section. The sample shape and desired dimensions are shown in Fig 3.2.

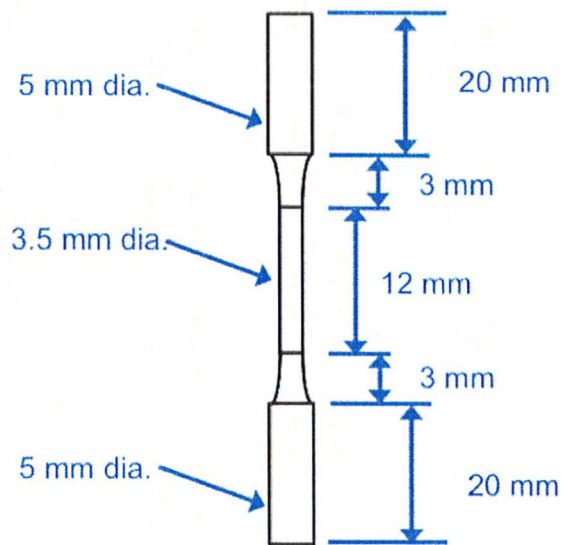


Fig 3.2 - Side view of cylindrical fatigue sample showing dimensions

Immediately before fatigue testing, the true dimensions of each sample were measured using a digital caliper. The gage length was measured by laying the sample in a grooved channel and measured as accurately as possible given the curvature of the transition between the gauge section and the grip sections. The diameter of the gage section was determined by measuring with digital calipers at several points along the gage length on two perpendicular axes until the smallest diameter was found. Once determined, this measurement was taken to be the sample's gage diameter, and the location carefully marked with a fine felt tip pen. Care was taken to avoid unnecessary contact between the

calipers and the sample as such contact could lead to the introduction of sharp gouges in the sample surface, which could act as stress concentrators.

3.2 S-N Fatigue testing of samples

3.2.1 Equipment and set up

Fatigue testing was performed on an MTS 858 servo-hydraulic tabletop tensile testing machine with Test Star IIs controller.

To set the testing machine correctly the caliper measurements of the current test sample are used to calculate the area of the sample, and thus the correct maximum and minimum loads required to apply the desired engineering stress to the sample. The dimensions are also loaded into the testing machine just prior to fatiguing, so that the program can automatically calculate the applied engineering stress and strains.

With the sample dimensions measured, the sample was loaded into the tensile tester. For this, the machine was first set in manual position control mode, and the upper and lower grips separated. The sample was placed in the lower grip, and at this point the load cell output was reset to be 0N. The upper grips were manually lowered to securely grip the upper grip section of the sample. The control mode was then set to manual load control, with the desired output set to 0N, and the upper grips were slowly closed on the sample. This method was employed to avoid any unintended applied loads on the sample

while the upper grip was closing, which could occur if the upper grip was closed under manual position control mode. The grips were closed as slowly as possible, allowing the actuator time to compensate for any axial force applied to the sample by the grip.

Once mounted in the grips, an MTS 1385314 extensometer was attached to the sample such that the contact points of the measurement knives lay on opposite sides of the narrowest gage diameter, as marked during the measurement process. The extensometer was mounted using small dental elastics, and aligned so that its measurement axis was parallel to the tensile axis. Care was taken while mounting the extensometer, as forces applied to the sample or bottom grip could cause the load cell to detect an applied force, which would cause the tensile tester to apply an undesired load through the sample. In addition, careless contact between the sample surface and the extensometer knives could produce undesired gouges in the sample surface. In mounting the extensometer it was important that the knives initial position be as near the middle of their deflection range as possible to ensure accurate readings. Once mounted, the extensometer output was calibrated to take that position as $\epsilon_a = 0$ mm/mm. At this point the tensile tester was taken off user-defined control mode, and the fatigue program was started.

3.2.2 Test specifications

The wheel spoke from which the samples were cut is loaded in a manner best approximated by axial loading during normal operation, and the samples were cut such

that their tensile axis matches that of the spoke. As such, S-N fatigue testing was carried out under conditions of stress controlled axial fatigue. For future samples from other parts of the wheel where loading conditions and sample orientation differ, other loading modes may be employed in future stress controlled S-N testing. The sample was loaded cyclically with a fully reversed sinusoidal stress profile, with a median stress of 0MPa, and the amplitude set to the desired test stress. Testing was continued until failure of the sample by rupture, and the number of cycles completed at rupture recorded for construction of the S-N profile.

Under ASTM E466-07 for S-N testing, valid S-N tests require that the maximum and minimum stress applied remain within 2% of the target stress double amplitude once the correct amplitude has been established. (ASTM, 2007) In order to accomplish this with an acceptable degree of certainty the S-N testing was performed at 4 Hz, and after each test the peak stress versus cycle data recorded was plotted and checked for any significant deviation, which would invalidate the results gathered. Another test criterion was that the duration of the period at the beginning of a test during which the applied load amplitude had not yet reached the target amplitude should be kept as short as possible. In the case of the tuning employed in this testing this initial period lasted approximately ten to fifteen cycles, which was a short enough duration as to not significantly impact the testing. Both these criteria were met by performing control system tuning of the tensile tester using samples from an as-cast billet of AZ80, which were machined using the same process and desired dimensions as the wrought samples from the hot forged wheel.

One concern was that the criteria for sample failure detection used by the fatigue program required several cycles to properly detect when a sample failed by complete rupture. As such, it was possible for the fracture surfaces of the two halves of a ruptured sample to strike one another as the actuator continued its motion for the cycles before the program detected the test had completed. In addition, after detecting the rupture the program would respond by shutting down the actuator causing the upper grip to slowly descend under gravity, and therefore still carried a risk of the fracture surfaces coming to rest against one another. The result of either form of contact was damage to the fracture surface, which would interfere with analysis. To solve this issue, a limit criterion in the main control program was utilized.

Limit criteria was set such that if the upper grip was detected to raise more than 8mm, which is several times the range of strain elongation occurring during normal cycling, the limit criteria would trigger the Program Hold command. This would hold any running program at its current step without halting operation. As the fatigue program would be operating in load control, the Program Hold command would be activated while program was in the tensile-loading portion of the load cycle, locking the desired load at a constant tensile value. After rupture the actuator would no longer interact with the load cell, and since the control system input was being maintained at a constant positive tensile value by the Program Hold command, the control system parameters would be left unsatisfied. Under these conditions, the testing machine would continue to raise the upper grip until it reaches its programmed maximum height, rather than cycling or deactivating

the actuator. At the maximum grip height the program would detect that there were no possible solutions remaining for the control system parameters, and would lock out all movement under load channel saturation conditions, holding the grip at the maximum height until overridden by an operator and preventing any contact between the two fracture surfaces.

During testing the program automatically records number of completed cycles, time passed since the beginning of the test, applied load in kN, strain detected by the extensometer, extension in millimeters as measured by the actuator, and calculated engineering stress. For a stored cycle, this data is recorded throughout the cycle, allowing the calculation of hysteresis curves and similar data for any recorded cycle. As S-N testing entails up to millions of cycles, the fatigue testing program only stores certain desired cycles in order to decrease the size of file required per test, using a step-logarithmic system. For each consecutive order of magnitude of cycles completed, the testing program will only store to file the data of ten equally spaced representative cycles. As such, the file of a test that lasts ten cycles will have ten stored entries, while the file of a test that lasted one thousand cycles would have thirty entries.

The program also utilizes a buffer to store the results of the last half of the completed number of cycles. When the test concludes, the same step-logarithmic system is applied to the buffered cycle data, starting from the final cycle and working backwards. The result is that there are many representative cycles from the beginning and end of the

test recorded, and few from the middle of the testing period. This process is desirable in that the size of stored files is reduced from millions of cycles of data to approximately two hundred representative cycles, while still providing a good representation of the fatigue test, as changes in the sample occur at the highest rates at the beginning of fatiguing during work hardening, and at the end as the sample approaches crack formation and rupture.

3.3 Sample preparation for SEM and TEM studies

3.3.1 SEM sample preparation

Some fatigued samples were selected for fracture surface analysis, based on the stress amplitude at which they were fatigued. From each of these fractured samples only the section with the shorter gage length of the two sample sections was prepared for study by scanning electron microscopy (SEM), so that the remaining portion could be used for study by transmission electron microscopy (TEM). In addition, care was taken to always preserve as much gage section as possible, in order to conserve the maximum amount of useful material as possible for TEM study.

For SEM work, the sample could be no longer than 1cm to ensure the sample could safely occupy the sample chamber, and so material was removed from the end opposite the fracture surface, as seen in Fig 3.3. This was performed through spark erosion cutting, using a dielectric oil submerged-sample spark cutter. Once the fracture

specimens were cut they were cleaned in an ultrasonic cleaner, using acetone. To prevent impact damage to the fracture surface, each specimen was cleaned separately in a plastic beaker. Specimens were then mounted on conductive stages using silver paint. Fracture surface observation was carried out on a Philips 515 SEM.

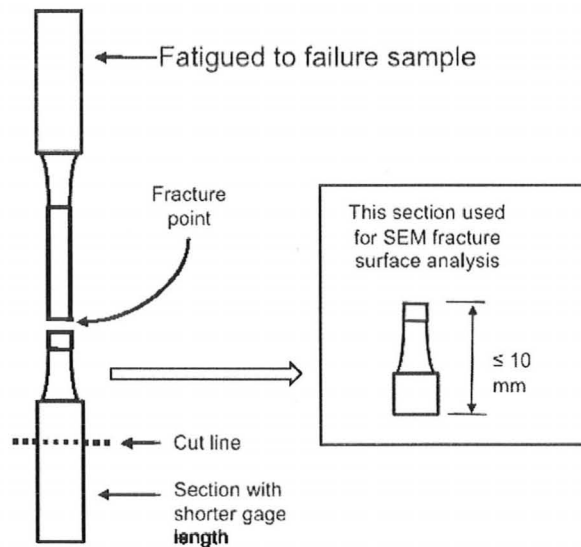


Fig 3.3 - Diagram of selection and preparation for fracture surface SEM

3.3.2 TEM sample preparation

Transmission electron microscopy (TEM) was used to view the microstructure and developed dislocation substructure in the samples. This required the preparation of electron transparent thin foils made from selected samples. Three samples were studied by TEM. The first had been fatigued at the highest stress amplitude tested, the second sample had been fatigued without failure for 9.6 million cycles and was considered to represent the endurance limit, and the third sample fatigued to failure at 1MPa above the endurance limit. To produce specimens for grinding and thinning into foils, the gage

sections of the fatigued samples were cut to produce disks, approximately 0.75 mm in thickness, perpendicular to the original sample's tensile axis. One disk from each sample, as well as one cut from a sample grip section prior to fatiguing, was used for X-ray Diffraction analysis (XRD) to compare the as forged texture to the texture developed under the varying fatigue conditions.

Cutting was performed using the same spark cutting device used to produce the fracture surface specimens, operated at the minimum available voltage potential in order to reduce the impact of the cutting process on the bulk material of the specimen disks. The disks were hand-thinned into foils by mechanical grinding using a gauged grinding holder. The target thickness for grinding was between 80 μ m and 90 μ m with material removed from both sides of the specimen disks. Kerosene was used as a lubricating agent, as exposure to water based lubricants was undesirable due to the reactivity of magnesium with water. From each disk one 3mm diameter foil was then punched, and foils were cleaned with acetone in an ultrasonic cleaner. After grinding, the foils were thinned to electron transparency thicknesses by jet electropolishing, carried out on a Struers TenuPol-5. The solution used contained 0.3g LiCl, 11.16g Mg(ClO₄)₂, 500 ml methanol, 100 ml 2-Butoxy-Ethanol. The electropolishing was conducted with the solution chilled to -53°C using liquid nitrogen, and at 60V applied. (Bettles, Gibson, Venkatesan, 2004)

After electropolishing, mild cleaning was performed using a Gatan Precision Ion Polishing System 691 Ion Mill, for 20 minutes at 2.1 kV. The 98MPa sample was cleaned

at $\pm 8^\circ$, while all other samples were cleaned at $\pm 6^\circ$, orientation off the sample plane and the incident ion beam. This was necessary to remove a layer of film, which had formed on the surface of the thinned foils. TEM studies were carried out using Philips CM12 electron microscope operating at 120 keV.

Chapter 4 - Experimental Results

4.1 S-N testing results

4.1.1 S-N curve

Figure 4.1 shows the S-N curve produced by testing samples from the spoke of the wrought Magnesium AZ80 wheel. As seen from the figure, the spoke material exhibits an endurance limit of 98MPa, well defined and bounded by a sharp bend in the S-N curve. At 99MPa the fatigue life was 54257 cycles, while at 98MPa the alloy exhibits fatigue life in excess of 9.6 million cycles.

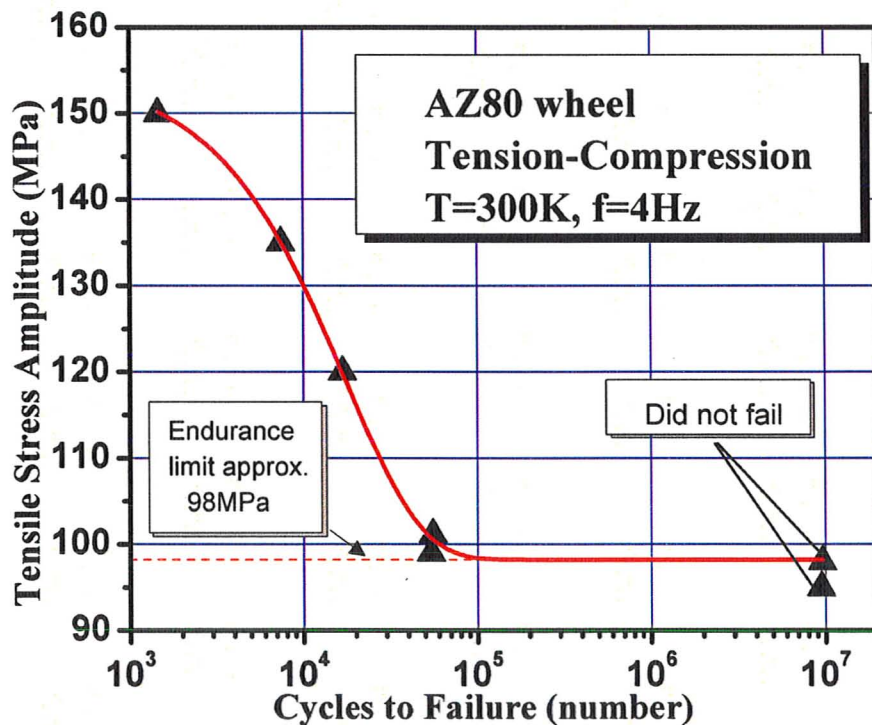


Fig 4.1 - Total life S-N curve for spoke material of wrought AZ80 magnesium alloy wheel

4.1.2 Accuracy of loading during testing

Figure 4.2 shows the peak applied tensile stress curves for each test, all samples maintained a variation in peak-to-peak amplitude of <2% of the target stress double amplitude, once the correct amplitude has been established. Thus, according to the ASTM E466-07 standard for S-N testing, the application of stress during S-N testing was valid.

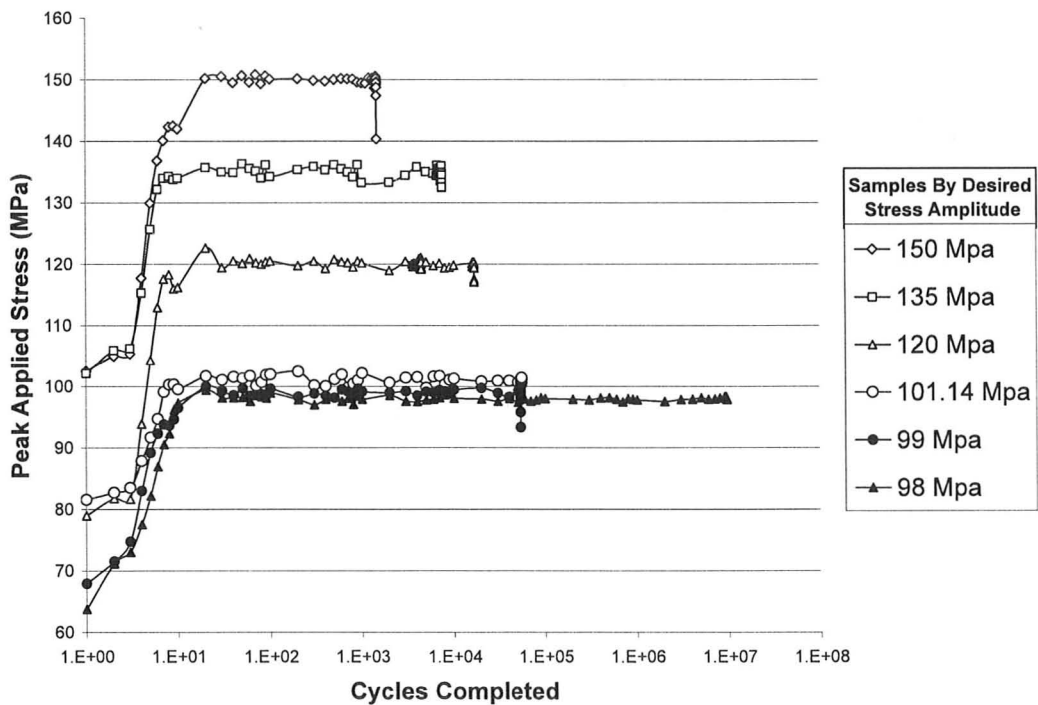


Fig 4.2 - Plot of Peak Tensile Stress Applied vs Cycles Completed for samples used in construction of S-N curve

4.1.3 Anomalous results

Some samples tested were deemed invalid and were not included in the S-N curve results. The conditions and fatigue life results of these samples are collected in Table 4.1.

In each case the samples were considered invalid as they failed in the grip section while fatiguing, due to over-tightened grips.

Table 4.1 - Testing condition and fatigue life results for samples considered invalid for S-N analysis

Sample Designation	Testing Stress Amplitude (MPa)	Fatigue life before invalid fracture
1-3	100	13483 cycles
1-5	90	13198 cycles
1-7	99	13378 cycles

4.2 SEM fracture surface observations

SEM microscopy of the fatigued fracture surfaces of three selected samples was carried out to characterize the general process of crack growth in the wrought AZ80 spoke material. These samples were: (i) the sample fatigued at the highest stress amplitude of 150MPa, (ii) the sample fatigued at an amplitude of 135MPa and (iii) the sample fatigued at a 99MPa amplitude which represents the lowest stress amplitude tested which induced failure. Selected SEM results are shown in Fig 4.3 to 4.9. The samples were aligned during imaging such that in all images the primary failure crack grew from left to right.

Observation of the 135MPa and 99MPa stress amplitude sample fracture surfaces shows that crack nucleation occurred at the surface of the samples. Each sample exhibits a limited quantity of fatigue striations showing that multiple cracks nucleated at the surface, then grew until merging into a unified crack front, as seen in the 135MPa sample shown in Fig 4.3.

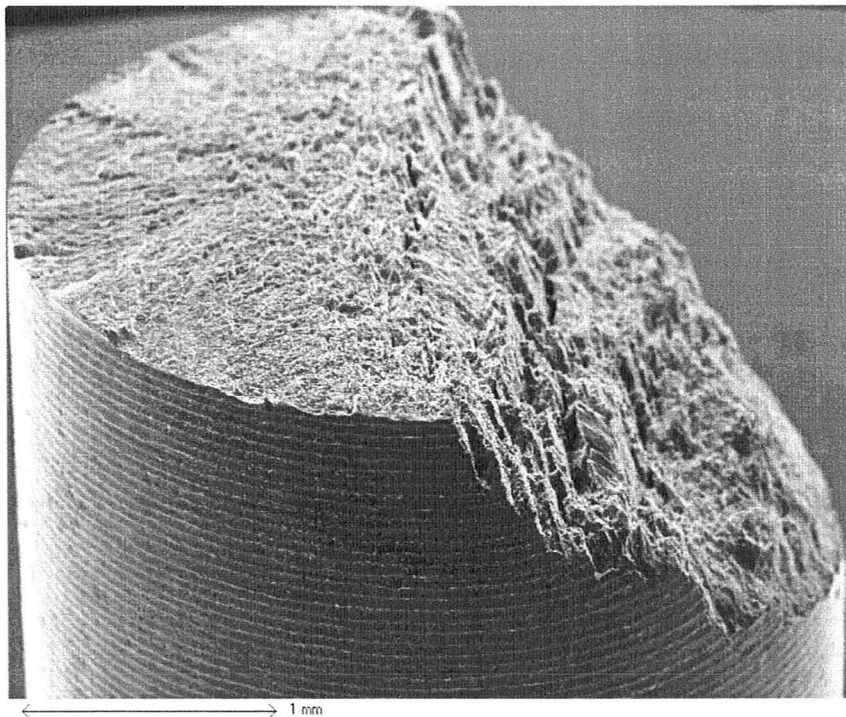


Fig 4.3 - Side view of surface fracture for 135MPa stress amplitude sample

The fracture surface of both samples contains evidence of both localized ductile and brittle fracture. The fracture was neither true brittle or true ductile fracture, and featured an opportunistic rapid cracking mode, which transitioned in the coarseness displayed as the crack grew. Near the crack nucleation point the sample was relatively smooth with minimal plastic deformation, forming a fine textured plane composed of

numerous small steps formed by rapid and largely brittle fracture, interspersed with some small voids and pits. This region also contained microscopic secondary cracks predominantly oriented such that their growth direction was closer to that of the tensile axis than of the primary crack growth, as seen in Fig 4.4 and Fig 4.5.

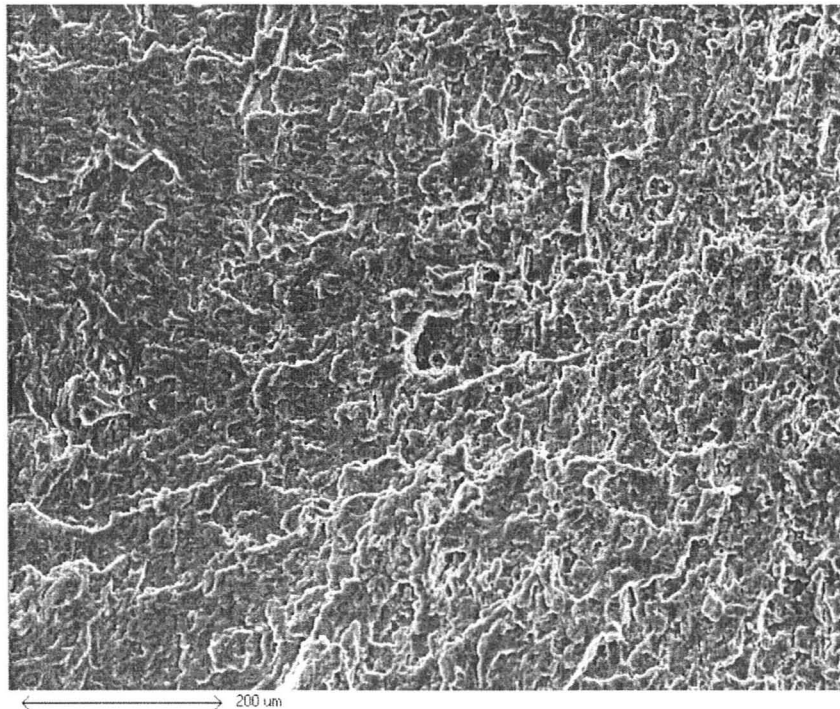


Fig 4.4 - Surface Texture near crack nucleation point on 135MPa sample

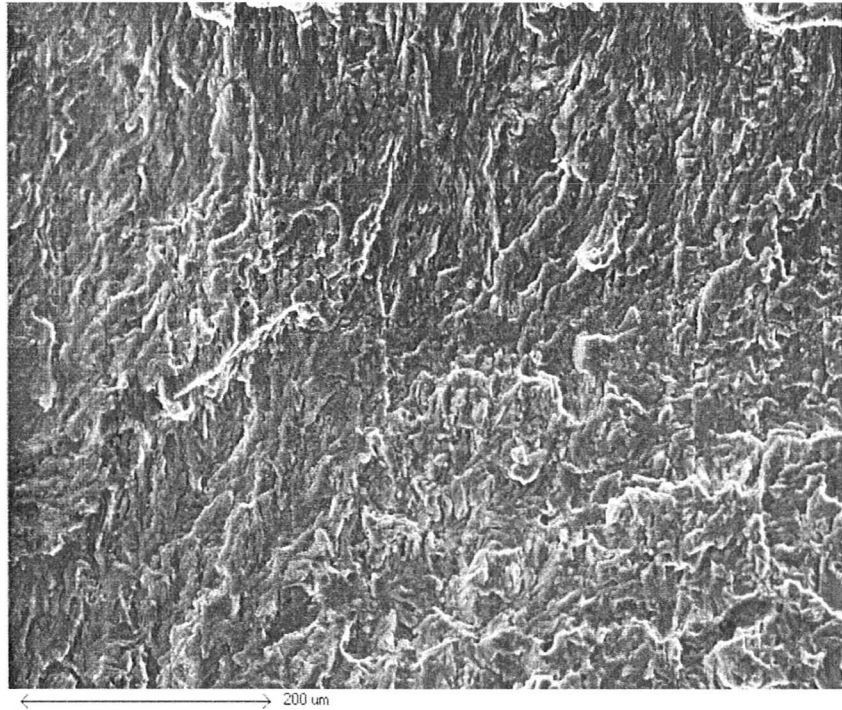


Fig 4.5 - Surface Texture near crack nucleation point on 99MPa sample

Along the direction of primary crack growth there is a clear gradual transition in surface texture, and observed features indicate an increasing coarseness of the stepped structures. This transition leads to a region dominated by increasingly coarse texture with larger stepped structures containing voids of various size and shallow dimples, as well as localized areas of plastic deformation of the fracture surface, interspersed with small regions of smooth stepped failure mode and secondary cracking features described above. As the length of the primary crack increased, the size of these secondary cracks also increased, with several wide enough to observe that they appear to be propagating in a direction approximately 30° - 40° off the tensile axis. This feature can be seen in Fig 4.6, below

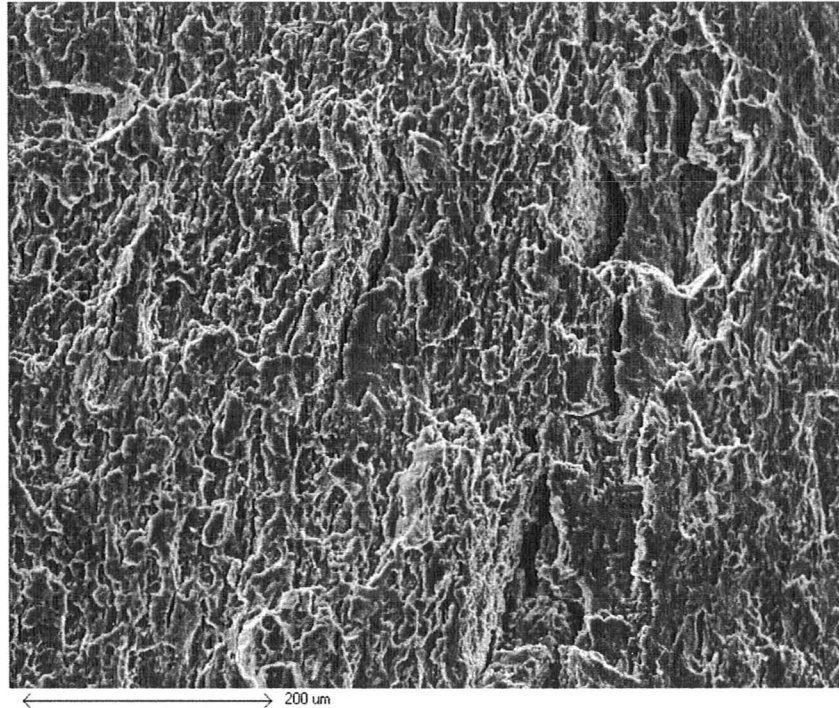


Fig 4.6 - Angled secondary cracking in 135MPa sample

Additionally, in both these samples the direction of fracture surface growth of all samples began perpendicular to the tensile axis. However, in the coarse region of surface texture described previously the plane of the crack growth sharply angled to a different plane approximately 40° to 60° , as seen in the 135MPa sample shown in Fig 4.3. This slope feature, seen in each fractured sample, contains relatively large regions of relatively smooth planes of crack growth or cleavage, similar to the smooth regions seen near the crack nucleation points, and surrounded by coarse failure regions.

These features are also present in the fracture surface of the 150MPa sample. However in this sample the region of smooth texture dominated by step-like cracking and interspersed secondary cracking seen near the crack nucleation point is smoother and

smaller as seen in Fig 4.7. The transition to larger step structures and coarser fracture texture also occurs earlier in the crack growth history than in the lower stress samples, but contains the same features, as seen in Fig 4.8. In addition, this sample also contains the slope feature seen in the other samples, containing intermixed regions of smooth and coarse fracture. However in the 150MPa sample this feature occurs closer to the crack nucleation point than in other samples, and unlike the other fracture surfaces this feature is not a singular instance comprising the remainder of the crack growth. Instead there is a series of these slope features, each smaller than those observed on the 135MPa and 99MPa fracture surfaces, and arranged in a manner similar to fatigue striations, as seen in Fig 4.9.

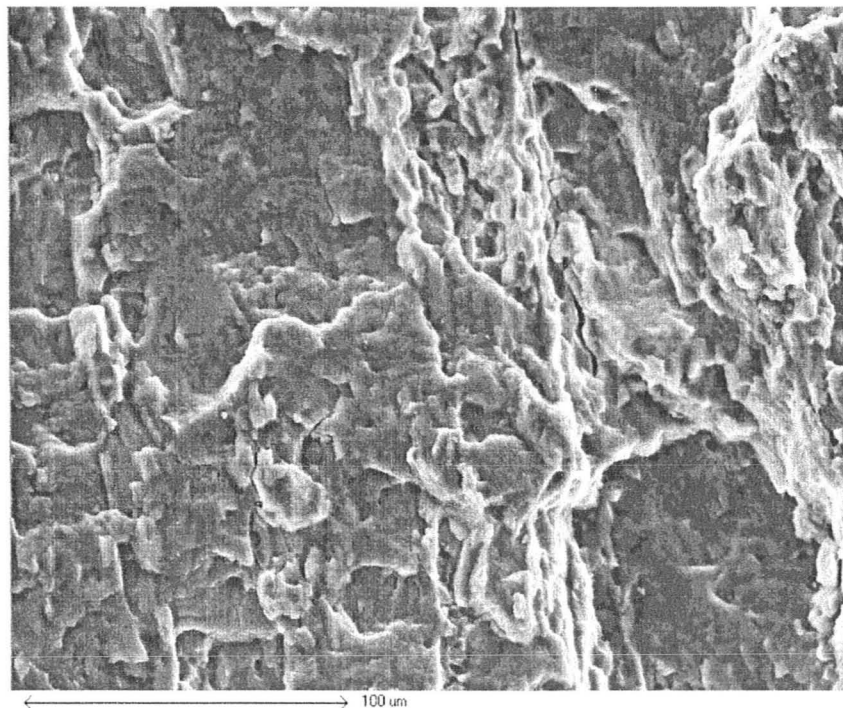


Fig 4.7 - Smooth region near crack nucleation point in fracture surface of 150MPa sample

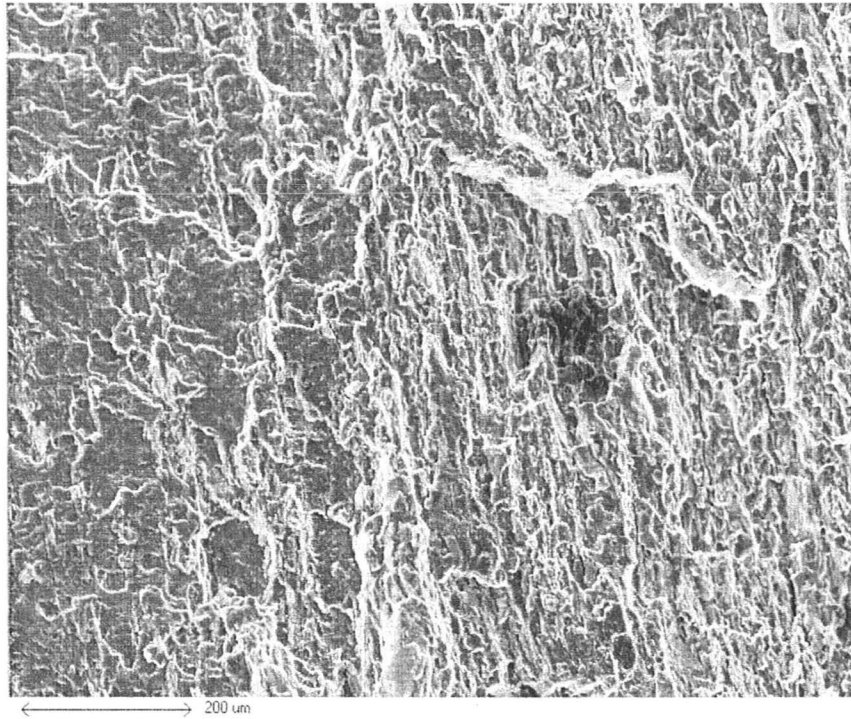


Fig 4.8 - Transition region towards increased step size in fracture surface of 150MPa sample

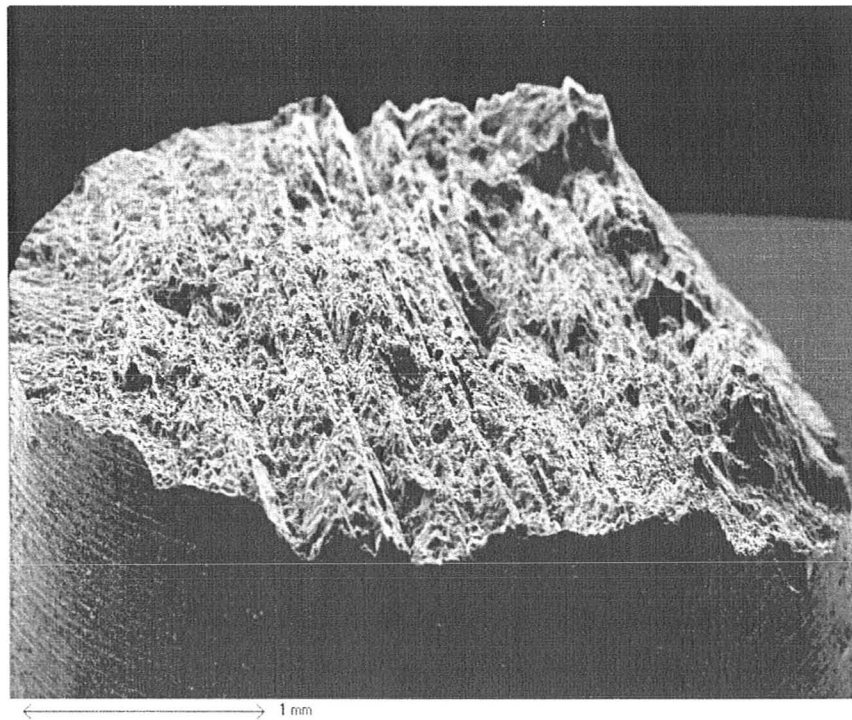


Fig 4.9 - Side view of surface fracture for 150MPa stress amplitude sample

4.4 Texture analysis

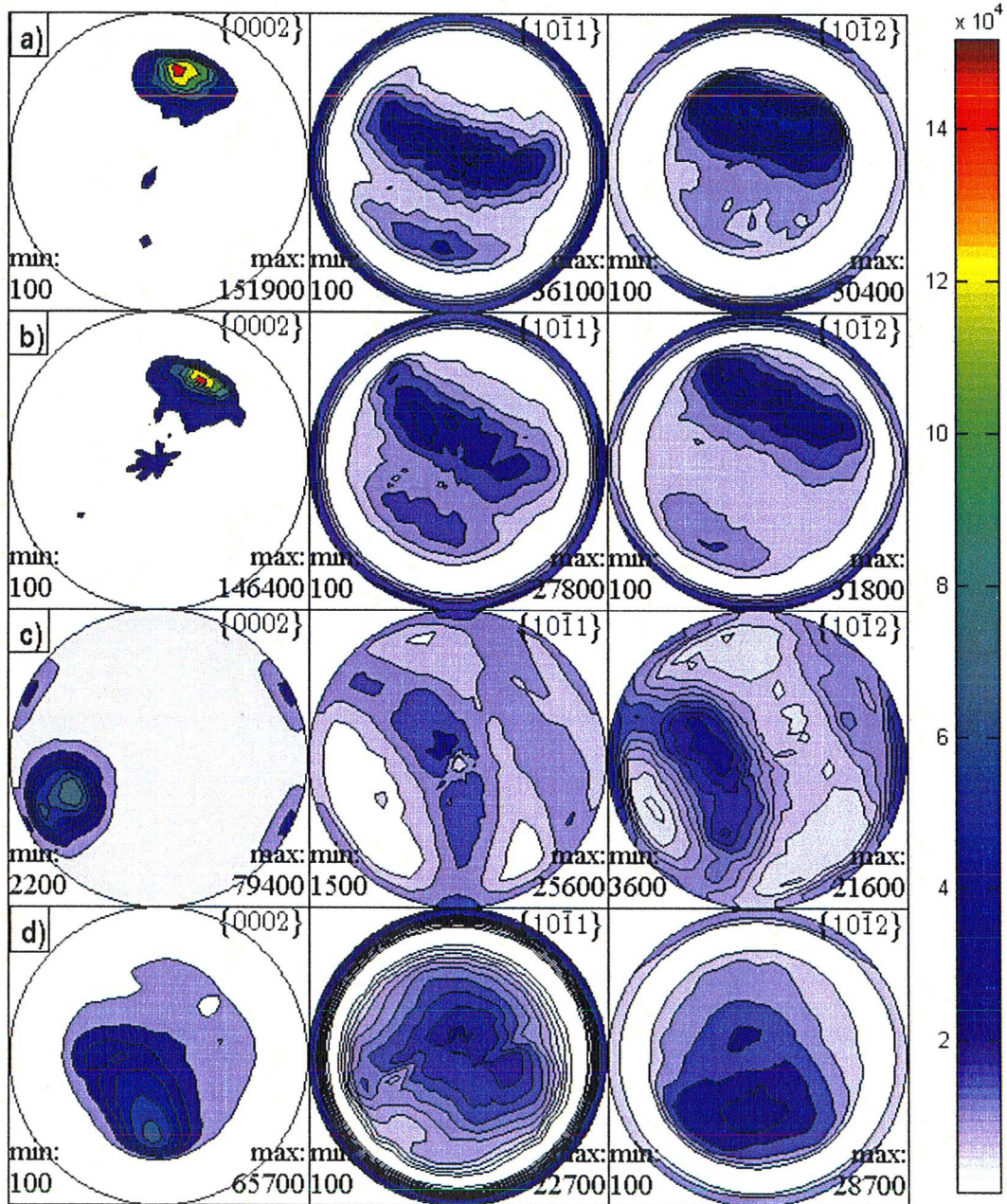


Fig 4.10 - Pole figured collected from samples fatigued at a) 150MPa, b) 99MPa, c)98MPa and an as-forged sample, d)

Pole figures collected from disks cut from as-forged and fatigued samples are shown in Fig 4.10. As the samples lack a defined rolling direction, it must be noted that relative differences in radial orientation between samples are an artifact of testing. Results show that there is a strong material texture in these samples, with the majority of grains oriented such that their basal plane is 40° to 60° off the tensile direction. As this is seen in the as-forged sample, this texture is likely the product of deformation during the forging process. However, results from the fatigued samples show a small refinement to this texture, with the orientation becoming more strongly represented after testing. Also of note, there is a difference in the degree of refinement between the 99MPa and 98MPa samples, which coincides with the endurance limit. No signs of mechanical twinning are observed.

4.5 TEM observation of microstructure

TEM imaging of material from select fatigued samples was performed to inspect the fatigued AZ80 wrought wheel microstructure. The samples selected represent: (i) the highest testing stress amplitude of 150MPa, (ii) the lowest stress amplitude of 99MPa at which failure occurred, and (iii) the non-fractured sample representing the endurance limit at 98MPa. No precipitates or phases other than solid solution α -phase have been imaged in post-fatigue analysis. Observations of diffraction patterns indicate that the orientation of the grains imaged was such that the basal plane was slightly inclined to the foil plane, implying that the dislocations imaged are lying within basal plane.

In the 150MPa fatigue amplitude sample, a network of linear dislocations was found on the basal plane. Observed in bright field, regions of the sample containing very high densities of dislocation debris and some dislocation loops structures are observed, as shown in Fig 4.11. Observation by dark field imaging technique reveals areas primarily containing short dislocation sections, which are approximately linear. Shown in Fig 4.12, these dislocation segments were aligned and arrayed into an intersecting network of dislocations on non-coplanar planes.

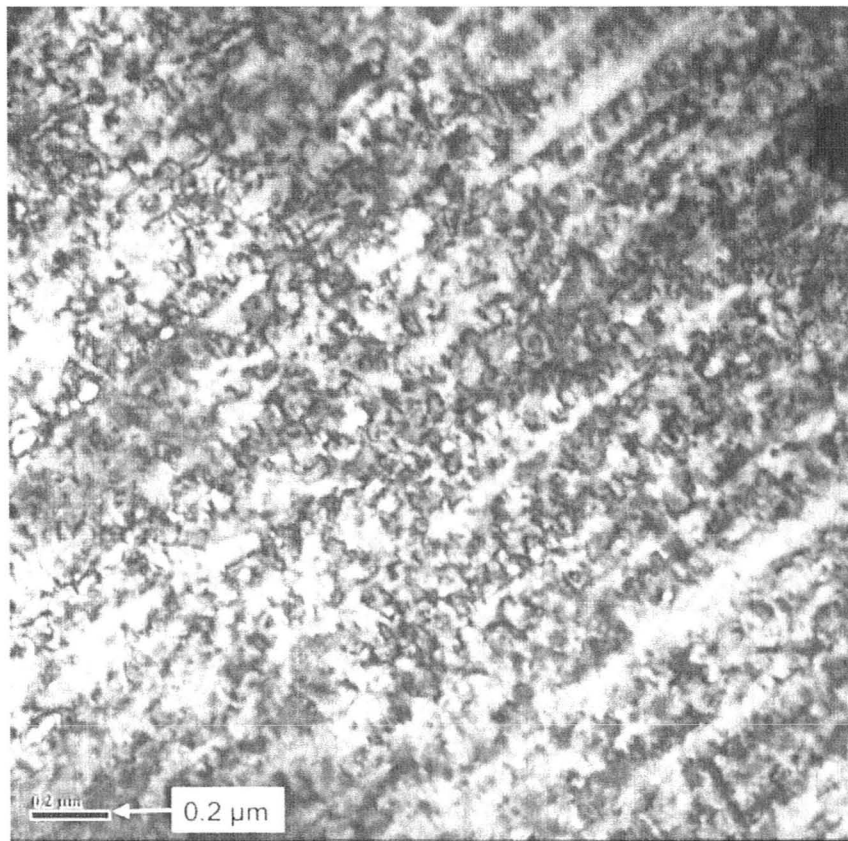


Fig 4.11 - Bright Field TEM of 150MPa sample showing densely packed loop dislocations and dislocation debris

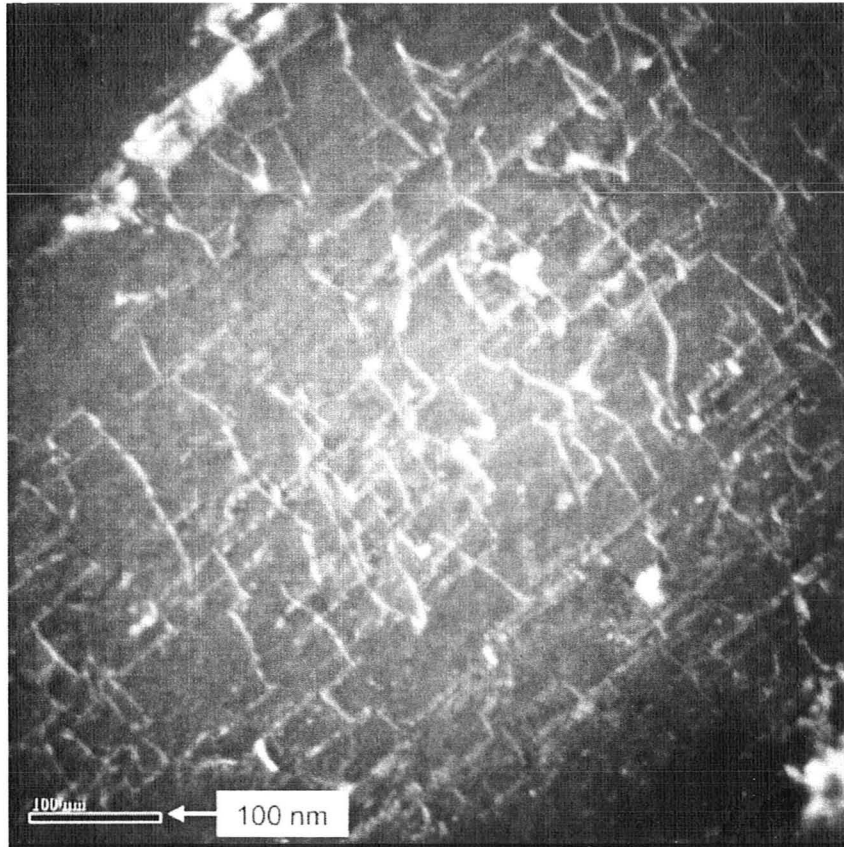


Fig 4.12 - Dark field TEM of 150MPa sample showing lattice-like dislocation array

Present on the basal plane of the 99MPa stress amplitude sample were an abundance of dislocation loop structures, as well as dislocation debris. In bright field and dark field, these loop structures are plentiful as seen in Fig 4.13 and Fig 4.14. Also viewed in dark field, the dislocation debris appears as smooth structures, and unaligned non-linear dislocations with segments in distended configurations as seen in Fig 4.15 and Fig 4.16 respectively. The lattice-like network of dislocations observed in the 150MPa sample was not observed in the 99MPa sample. Notable variation is apparent in the forms, sizes and orientations of the dislocations present in this sample. Also observed in this

sample were linear dislocations aligned near a grain boundary, intermingled with looped dislocation structures.

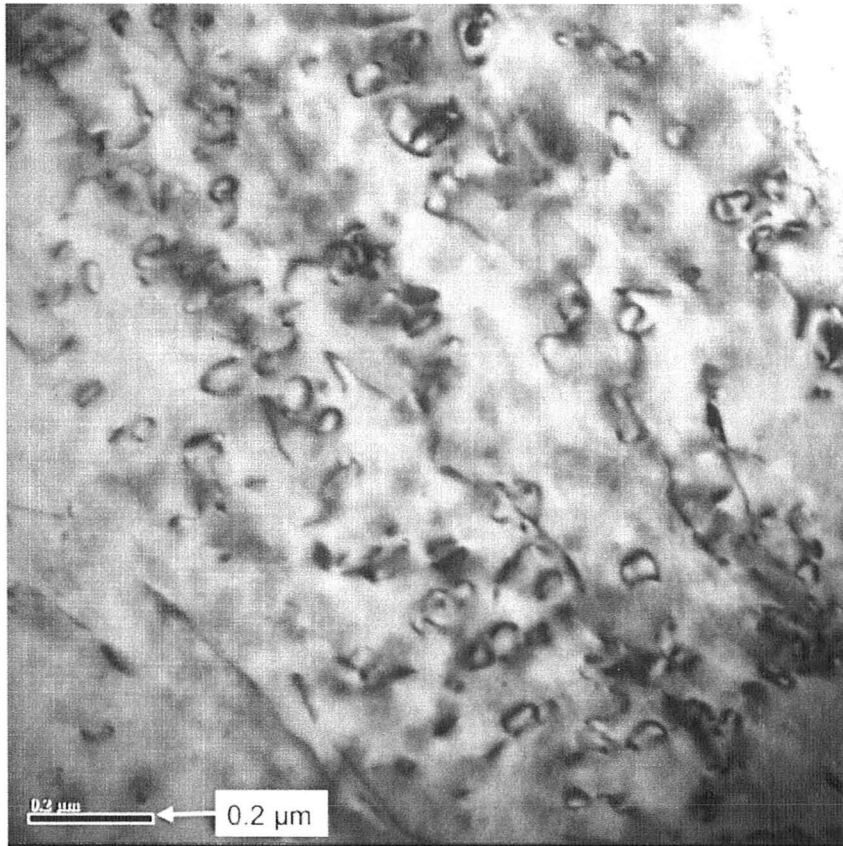


Fig 4.13 - Dislocation loops observed in bright field TEM of 99MPa sample

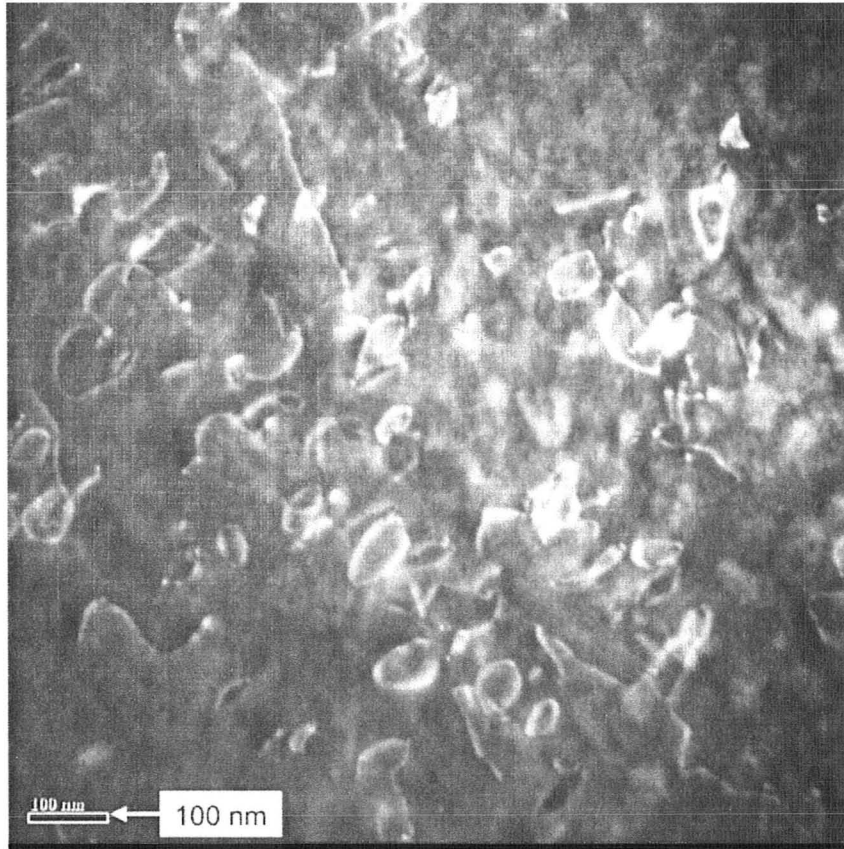


Fig 4.14 - Dislocation loops observed in TEM dark field of 99MPa sample

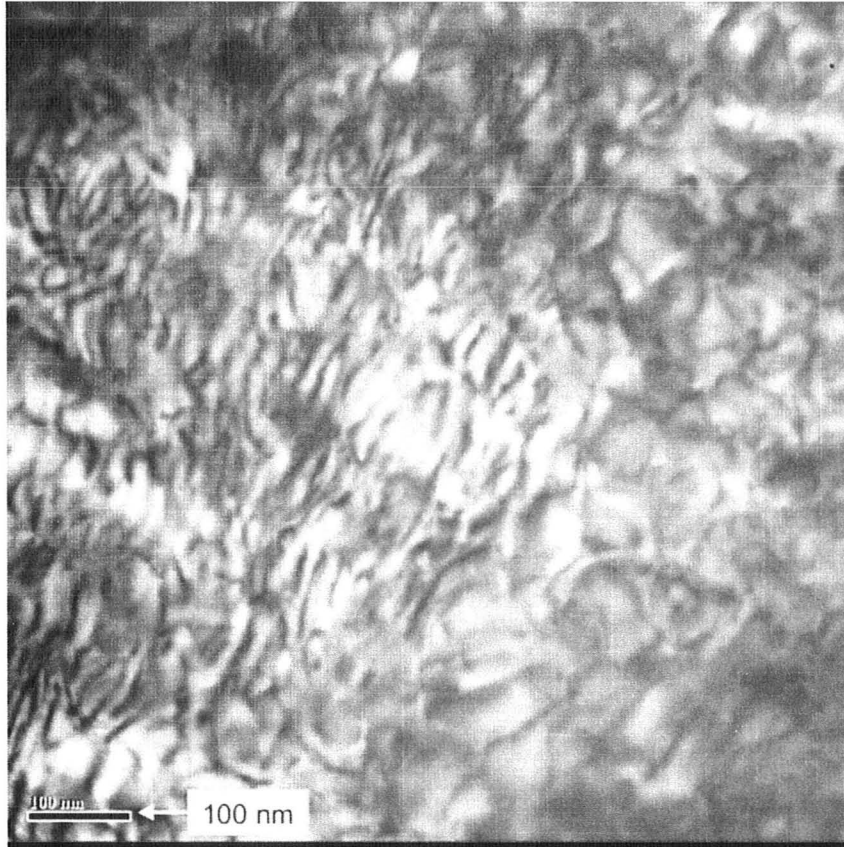


Fig 4.15 - Bright field TEM of dislocation substructure in 99MPa sample

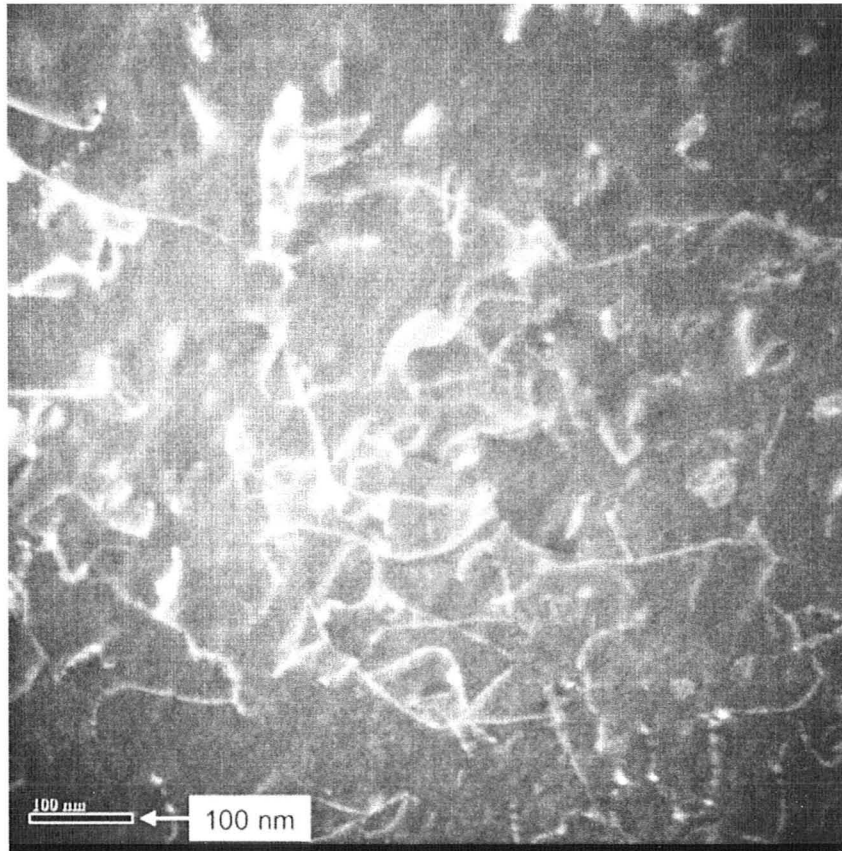


Fig 4.16 - Dark field TEM showing dislocation network in of 99MPa sample.

The 98MPa sample, which did not undergo failure, contained large amounts of small-scale refined dislocation debris, and some unaligned nonlinear dislocations randomly distributed throughout the volume of the material, as seen by dark field in Fig 4.17. Also viewed were non-linear dislocations with segments in distended configurations, as seen by dark field in Fig 4.18. Dislocation loop structures were rare, and those present were small. Of note are small defects seen dispersed throughout the material.

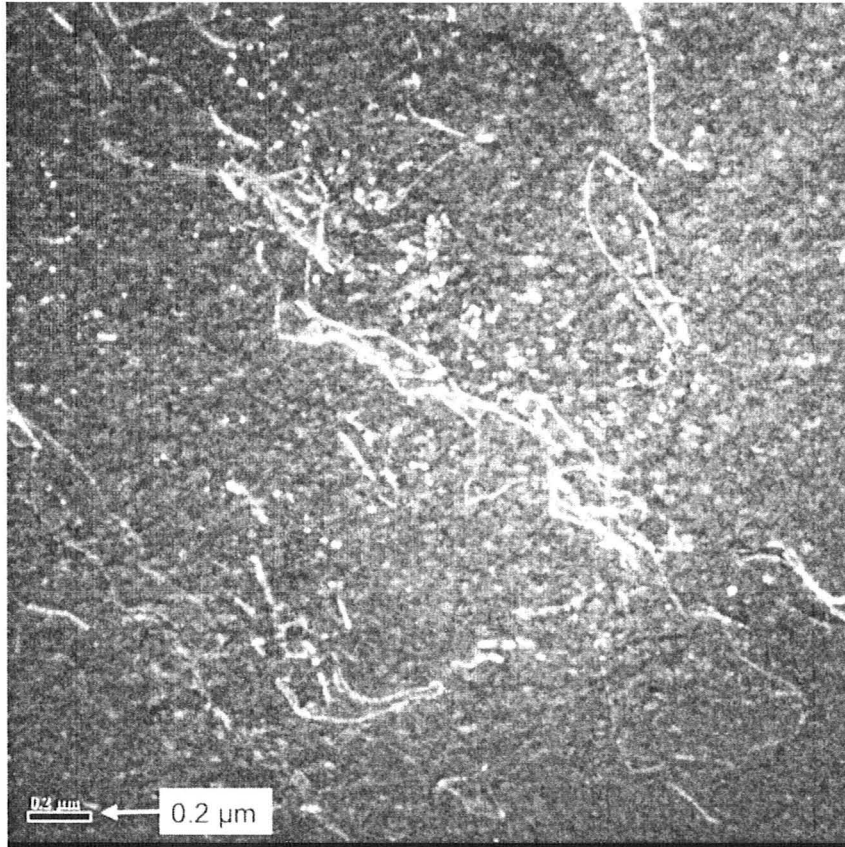


Fig 4.17 - Dark field TEM showing small dislocation debris and isolated dislocations in 98MPa sample.

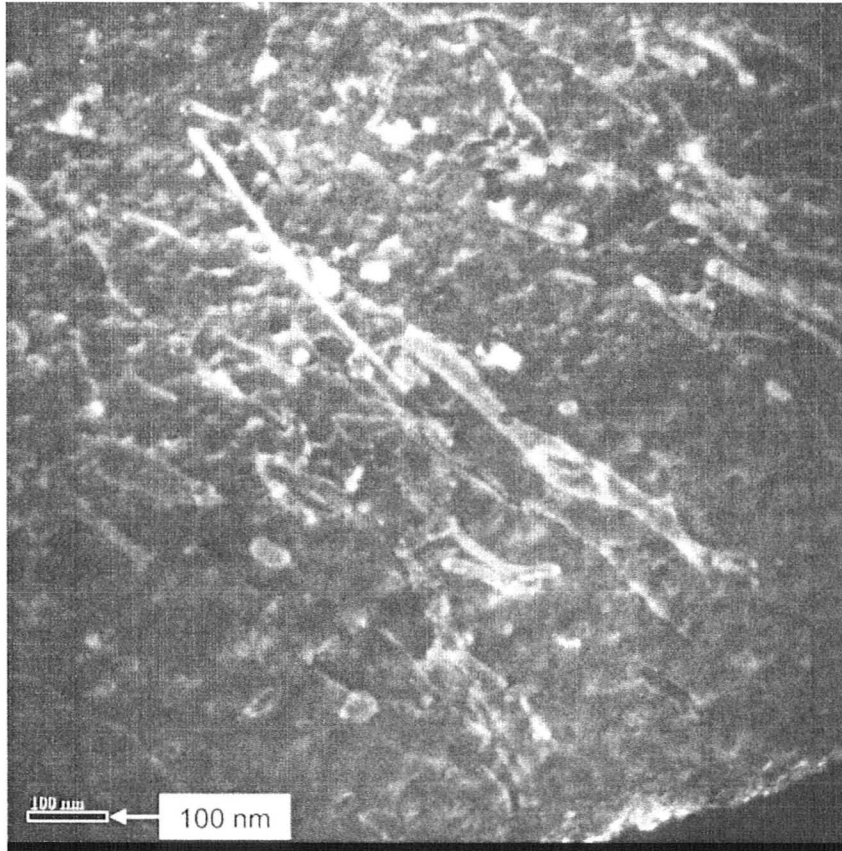


Fig 4.18 - Dark field TEM of 98MPa sample showing distended dislocation segments and sparse dislocation loops

Also observed in the 98MPa sample were loosely arrayed dislocations near a grain boundary, as well as aligned dislocations forming what appears to be a subgrain boundary, shown in Fig 4.19 and Fig 4.10 respectively.

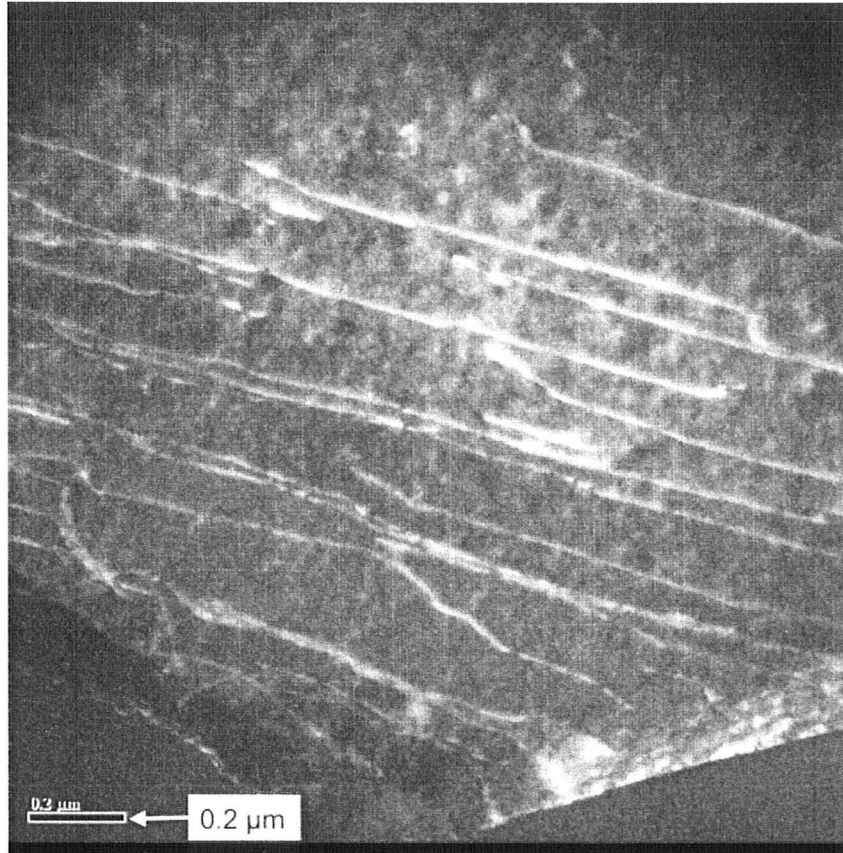


Fig 4.19 - Dark field observations of aligned dislocations near grain boundary in 98MPa sample

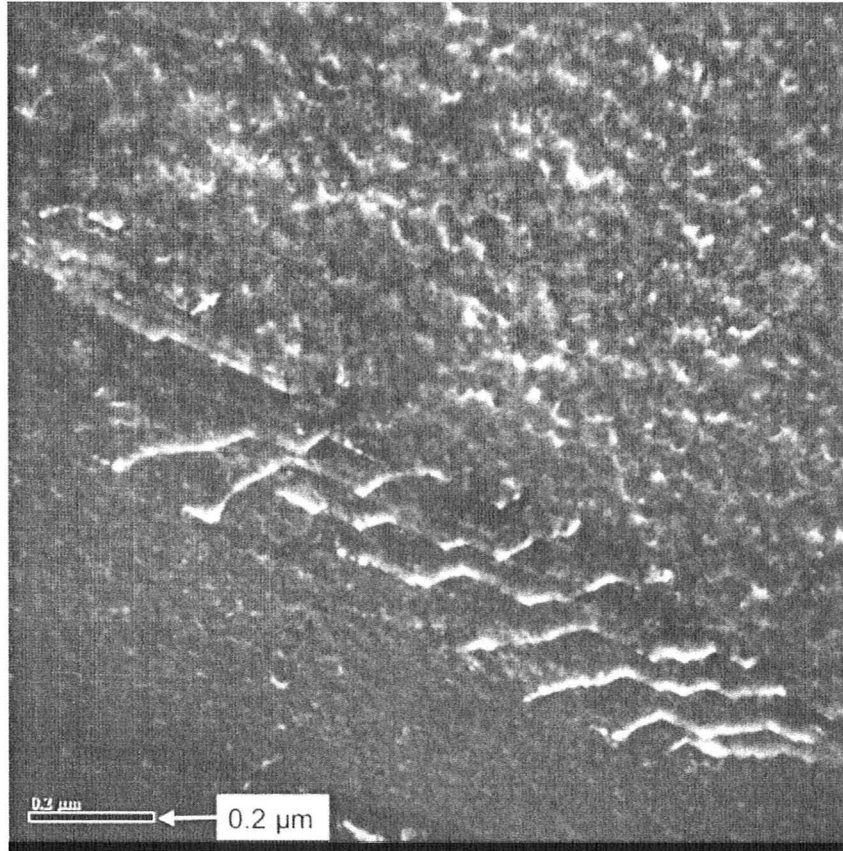


Fig 4.20 - Dark field of dislocations clustering at subgrain boundary in 98MPa sample

Chapter 5 - Discussion

Stress controlled axial loaded cyclic fatigue testing was performed on samples cut from spoke sections of a wheel composed of magnesium AZ80 produced through a hot forging process. The applied tensile stress amplitude vs fatigue life (S-N) curve, used to characterize material fatigue behaviour, was plotted.

In previous studies, the S-N curve was determined for several magnesium alloys under various manufacturing, surface finish and microstructure conditions carried out by several loading modes of stress controlled fatigue testing, including AZ80. (Nan et al. 2004, K.Tokaji et al. 2004, Shahzad et al. 2007, Hilpert and Wagner, 2000) In the case of the AZ80 alloys the authors found that the S-N curves contained a defined endurance limit, and did not contain a sharp bend. Additionally the AZ80 studies found that the microstructure conditions of the sample strongly influenced the fatigue life. In the present work the S-N curve for the forged AZ80 magnesium alloy was found to contain a sharp bend, and described a well-defined endurance limit of 98MPa applied stress amplitude. As a comparison, previous tensile testing of the samples by Diak (2009) found an engineering yield stress of approximately 109MPa, placing the observed endurance limit at 89.5% the observed $\sigma_{e, y, 0.2\%}$. In addition, previous FEA work by Ju (2008) found that the highest stress level expected in the wheel spoke is 14MPa, with the highest stress expected in the complete wheel to be 21.45MPa, both well below the 98MPa endurance limit found in the S-N curve.

The present results show that there is a clear distinction between the S-N curve found in the present work and those of previous studies, which implies the presence of a fatigue mechanism in samples of the forged spoke section AZ80 not present in the AZ80 material from previous studies. Tokaji et. al. (2004) and Nan et. al. (2004) found similar S-N curve results in magnesium AZ31 alloy produced under varying manufacturing processes, and suggested that the sharp bend and well defined endurance limit was caused by the presence at the endurance limit of a non-propagating crack being restrained by local microstructure phase interfaces. These cracks were observed to form rapidly and grow until meeting the interface, which would prevent the growth of the crack at stress amplitudes below the endurance limit, while at higher stress levels the interface would only slow the growth of the crack.

In contrast the AZ80 material in the present work, as observed, contained mainly a single solid solution α -phase with no readily apparent precipitates or inclusions, and shares this trait with the AZ80 material which exhibited different S-N curve behaviour in the earlier mentioned previous studies. As such, there are no observable phase interfaces available to inhibit the growth of cracks in the same manner as the AZ31 studies, and thus assuming an absence of a secondary phase the similar behaviour must have a different cause. However, secondary phases are likely present although not presently observed in the present work, as AZ80 lies beyond the solubility limit of aluminum in magnesium. Assuming the presence of β -phase structures there is now a phase interface, providing a

method for cracks to rapidly nucleate within the β -phase and become sessile upon reaching the interface.

If the sharp bend in the present AZ80 S-N curve is caused by a non-propagating crack at the endurance limit, it would likely be due to a microstructure which below a critical stress amplitude acts to impede the growth of cracks which exists in this wrought AZ80 material and not in the AZ80 seen in previous studies. It is also possible that this effect is due to the strong material texture present in this work, as this may inhibit crack growth or microstructure development during fatiguing. Alternatively, if a non-propagating crack is not present at the endurance limit, the sharp bend could be due to a microstructure or dislocation feature or process that impedes the initial nucleation of a crack below a critical 98MPa applied stress amplitude for this AZ80 material.

Observation of the fracture surfaces of samples fatigued for S-N testing via scanning electron microscopy was carried out using a Philips SEM 515. Results showed several features that can be used to estimate the crack growth process. Previous study by Srivatsan et. al. (1997) of the fracture surface of several fatigued magnesium alloys under strain control showed characteristic surface features displaying a mix of ductile and brittle fracture mechanics. Regions of stable crack growth displayed cracking extending into the material along grain boundaries running parallel to the major stress axis, while a region of tensile overload displayed ductile voids and dimples of various sizes as well as brittle fracture along grain boundaries. The authors also noted that the formation of micro and

macro cracks occurred at the end of the fatiguing process, as opposed to occurring early on in the fatigue process. Although the testing conditions and alloys are dissimilar, observation of the fracture surfaces in the present work reveal similar features, which could imply that the crack formation and growth processes involved are similar to those observed in previous work and that the sharp bend in the S-N curve is not caused by the growth of a rapidly nucleated crack being impeded, but rather the nucleation of cracks being impeded below a critical applied stress amplitude. If this were the case in the present work it would be expected that there would be a difference in the microstructure or dislocation substructure in the bulk material of AZ80 spoke samples fatigued at the endurance limit and of those fatigued above the endurance limit. Further study will be necessary to characterize the fatigue fracture behaviour of this material, and determine whether there is a non-propagating crack at the endurance limit.

Texture analysis was performed by X-ray diffraction (XRD), and showed the majority of the grains are orientated in the samples such that the (0001) direction is 40°-60° off the tensile axis in a distribution about a preferred radial direction. This result was found in the as-forged material and in the fatigued material, however the fatigued material displayed a slightly stronger texture with a smaller distribution in orientation. This implies that cyclic loading induced a small reorientation of grains towards this preferred 40°-60° orientation, but did not produce mechanical twinning deformation. Samples fatigued above the endurance limit showed a marked increase in this refinement when compared to the sample fatigued at the endurance limit, implying that this refinement

process, or the mechanism responsible for it, is likely involved in the critical-stress dependent mechanism producing the sharp bend in the S-N curve. In the present work the fracture surfaces were observed by SEM to each contain a feature in which the final portion of the fracture surface sharply sloped at approximately 40° to 60° to its original fracture plane, which was described by relatively smooth and flat fracture faces aligned to this 40° to 60° range making up sections of the slope, mixed with regions of more granulated texture. Combined, this implies that the crack may be growing until reaching a critical size at which the local stress is high enough to allow the crack to turn and use the (0001) plane as a cleavage plane. This is supported by the presence of multiple sloped cleavage plane features acting as fatigue striations in the 150MPa fracture surface. Further study will be required to characterize this fracture feature and determine if this is the case.

Dislocation substructure observation of thin foils produced from select stress control fatigued AZ80 spoke samples was carried out by transmission electron microscopy using a Philips CM12. The samples selected were the sample fatigued at the highest applied stress amplitude (150MPa), the sample fatigued at the endurance limit (98MPa) and the sample fatigued immediately above the endurance limit (99MPa). Results show that there is a distinct difference between the dislocation substructure above and below the endurance limit. While the 99MPa sample contains large quantities of dislocation loop structures closely packed on the basal plane, the 98MPa sample contains barely any dislocation loop structures. As this difference in dislocation development

coincides with a 1MPa applied stress amplitude differential which describes a well defined endurance limit featuring a sharp bend, it is reasonable to state that there could be a stress dependent dislocation process occurring in this AZ80 material which, above a critical applied stress amplitude, causes the dislocations to exhibit non-recoverable plastic deformation, resulting in the development of cumulative structures such as the observed loop formations. Previously, Stevenson and Vander Sande (1974) observed pure magnesium single crystals under strain controlled cyclic fatigue and observed that low strain amplitudes produced largely single slip deformation while high strain amplitudes produced increasing degrees of duplex slip. Similar processes may be happening in the present work, by which higher stresses cause other slip planes to become active, causing interactions between the various slip systems. Examples of other explanations include cross-slip occurring at high stresses causing parts of dislocations to become pinned on other slip planes during stress cycling, or the stresses reaching a critical amplitude at which they allow the formation of Frank-Reed loop dislocation sources. Further study of the dislocation substructures for these samples will be required to fully characterize the observed dislocation types, and to characterize the dislocation development process and determine the nature of its influence, if any, on the observed sharp bend in the S-N curve.

In previous studies stress controlled and strain controlled fatigue life testing was performed on several magnesium alloys, including AZ80, using material produced through differing manufacturing processes and with differing microstructure orientation to test the effects of microstructure characteristics on fatigue life and behaviour. (All Refs

Here) Results clearly showed a strong influence by the microstructure present. Hirsh and Lally (1965) showed that a slip system displays peak activation when the angle of slip lies between 40° to 60° off the tensile direction. In the present work, it was shown by XRD that there is a strongly preferred grain orientation of the basal plane distributed in a 40° to 60° range, implying that a majority of grains in the AZ80 wrought wheel spoke section samples are oriented such that basal slip is preferentially activated. This orientation, combined with the low CRSS of basal slip in HCP metals, likely exhibits a strong influence over the material fatigue behaviour and may also play a role in the mechanism which is producing the atypical sharp bend in the S-N curve. A peak activation of basal slip may act to limit the activation of other slip systems, possibly reducing the amount of irrecoverable dislocation processes occurring during cyclic loading and increasing the fatigue life. However, this orientation may also provide a means of critical failure as failure by cleavage becomes possible. Interestingly, the act of axial fatiguing appears to refine this texture, likely through unobserved twinning and kinking processes or the formation of subgrain boundaries, acting to enhance the average activation of basal slip during cyclic loading. This refinement is also less prominent in the endurance limit sample, which implies that the refinement process is influencing the fatigue behaviour and may be contributing to the formation of the sharp bend in the S-N curve. Further characterization of the effect of this material texture will be necessary to determine the influence imparted on fatigue life, and whether this texture refinement through cyclic loading is a beneficial feature of this material microstructure.

As other sections of the wheel have undergone different deformation histories and cooling rates throughout the forging process, they will contain differing microstructure from the spoke sections. As such it is necessary to perform further S-N testing on material representative of these other sections, to fully characterize the influence the forging process is imparting on the fatigue behaviour of the magnesium AZ80 alloy.

Chapter 6 – Summary and Conclusions

S-N testing of samples cut from the spoke section of a magnesium AZ80 wheel produced through a hot forging process was performed. Results showed a well-defined endurance limit at 98MPa, and a sharp bend in the S-N curve not seen in previous studies into fatigued AZ80 fatigue behaviour. Texture analysis showed an initial preferred orientation such that basal slip was preferentially activated, and refinement was seen after fatiguing likely imparting a strong influence on fatigue life, although further characterization is required to determine the extent and nature of the influence and whether it is beneficial. TEM analysis of dislocation substructures showed a distinct difference in dislocation development between material fatigued at the endurance limit and material fatigued 1MPa above the endurance limit. Similarly it was noted that, between the samples fatigued at the endurance limit and material fatigued 1MPa above the endurance limit, there is a marked degree in the fatigue-induced refinement of a preferred basal orientation. These differences are suggested as a possible cause of the sharp bend in the S-N curve. Further characterization via TEM is necessary to determine if this is the case, and to determine what process is causing the sudden appearance of these microstructure behaviours and how they relate to the critical-stress controlled fatigue behaviour observed. Further study to characterize the fatigue fracture process of the material is also necessary, to determine if there is a non-propagating crack at the endurance limit, and to determine if the sharp change in slope of the crack growth is due to a cleavage plane caused by the preferred basal orientation. Finally, further S-N testing

is required to characterize the fatigue behaviour of material from other sections of the wrought magnesium AZ80 wheel, as the forging process will impart differing microstructure throughout the wheel, which will in turn produce varying fatigue behaviour throughout.

References

ASTM (2007) ASTM E466-07

Bettles C.J., Gibson M.A., Venkatesan K., (2004), Scripta Mater, **51**, 193

Chen L. et al., (2007), Metall. Trans., **38A**, 2235-2241.

Courtney, T. H., (2000), Mechanical Behavior of Materials, McGraw-Hill Higher Education, 588.

Diak B., (2009), unpublished internal project report.

International Organization for Standardization, (1964), Geneva.

Hilpert M. and Wagner L., (2000), Journal of Materials Engineering and Performance, **9(4)**, 402-407.

Hirsch P.B. and Lally J.S., (1965), Phil. Mag., **12**. 595.

Hiura F., (2010), Master Thesis, McMaster University.

Hull D. and Bacon D.J, (2001), Introduction to Dislocations (4th Edition), Elsevier Butterworth-Heinemann.

Hutchinson W.B. and Barnett M.R., (2010), ACTA Materialia.

Ju F, Xia Z, Diak B J, Ojo O, MacDonald W D, Niewczas M. (2008), Magnesium Technologies, SP-2205. SAE International.

Kainer K.U., (2003) Magnesium Alloys and Technologies, Wiley-VCH.

Li F., Wang Y., Chen L., Liu Z., Zhou J., (2005), Journal of Materials Science, **40**, 1529-1531.

Nan Z., Ishihara S., Goshima T. and Nakanishi R., (2004), Department of Mechanical and Intellectual System Engineering, Toyama University, ECF15.

Sachs N., (2004), www.maintenanceworld.com.

Shahzad M., Eliezer D., Gan W., Yi S. and Wagner L., (2007), Trans Tech Publications.

Srivatsan T.S., Wei L. and Chang C.F., (1997), *Engineering Fracture Mechanics*, **56**, No. 6, 735-758.

Stevenson R. and Vander Sande J.B., (1974), *ACTA Metallurgica*, **22**, 1079.

Suresh S., (1991), *Fatigue of Materials*, Cambridge Solid State Science Series.

Tokaji K., Kamakura M., Ishiizumi Y., and Hasegawa N., (2004), *International Journal of Fatigue*, **26**, 1217-1224.

Transportation Safety Board of Canada, (2008), *Railway Investigation Report R06C0104*.

Von Mises R. and Angew Z., (1928), *Math. Mech.*, **8**, 161.

Yoo M.H., (1981), *Metall. Trans.*, **12A**, 409.

Yoo, Morris, Ho and Agnew, (2002), *Metall. Trans.*, **33A**, 813-822.

Zenner H., Renner F., (2002), *International Journal of Fatigue*, **24**, 1255-1260.

Zhang P., Lindemann J., Kiefer A. and Leyens C., (2005), *9th International Conference on Shot Peening*.

Zhang P., Lindemann J., (2005), *Scripta Materialia*, **52**, 485-490.

Zúberová Z. et al., (2007), *Metall. Trans.*, **38A**, 1934-1940.